

**NASA SOLAR SR&T PROGRAM  
CONTRACT NASW-03008**

**Modeling the Magnetic and Thermal Structure of Active Regions**

**FIRST SEMI-ANNUAL FIRST YEAR PROGRESS REPORT**  
Covering the period January 14, 2003 to July 13, 2003

Submitted by:

**Zoran Mikić**  
Principal Investigator  
Science Applications International Corporation  
10260 Campus Point Drive  
San Diego, CA 92121

October 7, 2003

## FIRST SEMI-ANNUAL FIRST YEAR PROGRESS REPORT

This report covers technical progress during the first six months of the first year of NASA SR&T contract "Modeling the Magnetic and Thermal Structure of Active Regions," NASW-03008, between NASA and Science Applications International Corporation, and covers the period January 14, 2003 to July 13, 2003. Under this contract SAIC has conducted research into theoretical modeling of the properties of active regions using the MHD model.

### Publication in The Astrophysical Journal

The publication "Coronal Mass Ejection: Initiation, Magnetic Helicity, and Flux Ropes. I. Boundary Motion-Driven Evolution," by T. Amari, J. F. Luciani, J. J. Aly, Z. Mikić, and J. A. Linker, has appeared in *The Astrophysical Journal*, **585**, 1073 (2003).

**Abstract.** In this paper we study a class of three-dimensional magnetohydrodynamic model problems that may be useful to understand the role of twisted flux ropes in coronal mass ejections. We construct in a half-space a series of force-free bipolar configurations with different helicity contents and bring them into an evolution by imposing to their footpoints on the boundary slow motions converging toward the inversion line. For all the cases that have been computed, this process leads, after a phase of quasi-static evolution, to the formation of a twisted flux rope by a reconnection process and to the global disruption of the configuration. In contrast with the results of some previous studies, however, the rope is never in equilibrium. It thus appears that the presence of a rope in the pre-eruptive phase is not a necessary condition for the disruption but may be the product of the disruption itself. Moreover, the helicity keeps an almost constant value during the evolution, and the problem of the origin of the helicity content of an eruptive configuration appears to be that of the initial force-free state. In addition to these numerical simulations, we report some new relations for the time variations of the energy and the magnetic helicity and develop a simple analytical model in which the magnetic field evolution exhibits essential features quite similar to those observed during the quasi-static phase in the numerics.

A reprint of this paper is included in Appendix A.

### Presentation at the Spring AGU/EGS Meeting, Nice, France

Zoran Mikić presented a paper at the Spring AGU/EGS Meeting, which was held in Nice, France, April 7–11, 2003:

- *Simulation of CMEs Originating in Active Regions*  
Z. Mikić, J. A. Linker, P. Riley, and R. Lionello

**Abstract.** Previously we have addressed the initiation of CMEs by large-scale changes in the solar photospheric magnetic flux. These CMEs had a global nature, since their size was comparable to the solar radius. These early investigations were primarily focused on the theoretical aspects of CME initiation, and the models were thus rather idealized. We will describe recent advances in our computational models

that have extended our capability to study localized CMEs, such as those that might originate from an active region. This capability will allow us to analyze actual CME events, and to compare our results in detail with CME observations.

This paper is included in Appendix B.

#### **Presentation at the Solar Physics Division Meeting, Columbia, Maryland**

Yung Mok presented a paper at the Solar Physics Division Meeting, which was held in Columbia, Maryland, June 16–20, 2003:

- *Parametric Dependence of Coronal Heating Mechanisms and Active-Region Emissions*

*Y. Mok, R. Lionello, Z. Mikić, and J. A. Linker*

**Abstract.** The thermal structure of an active region depends on the mechanism that heats the coronal plasma. A number of coronal heating mechanisms have been proposed over the years. They have different parametric dependences on the magnetic field, plasma density, and possibly other variables. Different mechanisms result in different thermal structures, and therefore, different EUV and soft X-ray emissions from an active region. Hence, the comparison between the computed emissions based on these models and the observed emissions will help to discover the parametric dependences of the actual heating mechanism and put some restrictions on the theoretical models. We have developed a 3D thermo-magnetohydrodynamic code to compute the thermal structure of an active region. The emissions resulted from various heating models will be compared with the images obtained from SOHO and Yohkoh.

This paper is included in Appendix C.

## **APPENDIX A**

**“Coronal Mass Ejection: Initiation, Magnetic Helicity, and Flux Ropes.**

**I. Boundary Motion-Driven Evolution”**

**T. Amari, J. F. Luciani, J. J. Aly, Z. Mikić, and J. A. Linker**

***The Astrophysical Journal*, **585**, 1073 (2003)**

## CORONAL MASS EJECTION: INITIATION, MAGNETIC HELICITY, AND FLUX ROPES. I. BOUNDARY MOTION-DRIVEN EVOLUTION

T. AMARI, J. F. LUCIANI, AND J. J. ALY<sup>1</sup>

Centre National de la Recherche Scientifique, Centre de Physique Théorique de l'Ecole Polytechnique, F-91128 Palaiseau Cedex, France;  
amari@cphpt.polytechnique.fr

AND

Z. MIKIC AND J. LINKER

Science Applications International Corporation, 10260 Campus Point Drive, San Diego, CA 92121

Received 2002 July 12; accepted 2002 October 10

### ABSTRACT

In this paper we study a class of three-dimensional magnetohydrodynamic model problems that may be useful to understand the role of twisted flux ropes in coronal mass ejections. We construct in a half-space a series of force-free bipolar configurations with different helicity contents and bring them into an evolution by imposing to their footpoints on the boundary slow motions converging toward the inversion line. For all the cases that have been computed, this process leads, after a phase of quasi-static evolution, to the formation of a twisted flux rope by a reconnection process and to the global disruption of the configuration. In contrast with the results of some previous studies, however, the rope is never in equilibrium. It thus appears that the presence of a rope in the preeruptive phase is not a necessary condition for the disruption but may be the product of the disruption itself. Moreover, the helicity keeps an almost constant value during the evolution, and the problem of the origin of the helicity content of an eruptive configuration appears to be that of the initial force-free state. In addition to these numerical simulations, we report some new relations for the time variations of the energy and the magnetic helicity and develop a simple analytical model in which the magnetic field evolution exhibits essential features quite similar to those observed during the quasi-static phase in the numerics.

*Subject headings:* MHD — stars: coronae — stars: flare — stars: magnetic fields —  
Sun: coronal mass ejections (CMEs) — Sun: flares

*On-line material:* color figures

### 1. INTRODUCTION

The problem of the nature of the triggering of coronal mass ejections (CMEs) has attracted considerable interest in the last few years. Priest & Forbes (2001) present an interesting review of the many observations constraining a pre-eruptive configuration. They stressed, in particular, two aspects that will be at the center of this paper: (1) shear is seen to be present in the chromosphere by the observations in H $\alpha$  of the fibrils (Tanaka & Nakagawa 1973) and along the inversion line of the normal component of the magnetic field (Hagyard et al. 1982; Machado & Moore 1991; Hagyard 1990), and (2) converging motions toward the inversion line have been observed, and they may increase the shear in a presheared magnetic configuration.

Another important feature observed in a relatively large number of CMEs is the presence of a prominence (Priest & Forbes 2001) and the ejection of a plasmoid, probably at the origin of the magnetic cloud sometimes observed afterward in the interplanetary medium (Burgala et al. 1981; van Driel-Gesztelyi, Schmieder, & Baranyi 2002). These coronal structures contribute in different ways to the total magnetic helicity. Twisted flux ropes have been often thought to be good candidates for explaining the coronal helicity content and budget and for triggering the eruptive events (Low 1994; Amari et al. 1999c, 2000). However, one important

issue has not been settled yet: is it really necessary to have a twisted flux rope (in equilibrium) prior to the disruption (Amari et al. 2000; Linker et al. 2001), or is the latter created as a consequence of reconnection during the disruption itself (Antiochos, DeVore, & Klimchuk 1999). It is worth noticing that these considerations do not exclude a priori one or the other topology since both the sheared arcade and the twisted flux rope may be sources of magnetic helicity exchange between the convection zone and the corona (there is conservation of the total helicity contained in the domain convection zone + corona, which is filled up with highly conducting plasma).

Modelizations of the triggering of CMEs have mostly concentrated on the problem of the evolution of a magnetic field occupying some unbounded domain (generally either a half-space or the exterior of a sphere) and embedded in very tenuous highly conducting plasma, this evolution being driven by slow (compared to the Alfvén velocity) motions of the footpoints. Initially, the efforts have concentrated on axisymmetric arcades submitted to purely shearing boundary motions. This problem has been treated in both Cartesian (Aly & Amari 1985; Aly 1990; Amari et al. 1996a, 1997 and references therein) and spherical geometry (Mikic & Linker 1994; Aly 1995), the evolution being found in each case to lead to the formation and ejection of a plasmoid once a sufficient shear has been applied. The effects of converging motions have also been considered analytically in the Cartesian case, and the existence of a catastrophic non-equilibrium transition was obtained (Priest & Forbes 1990;

<sup>1</sup> CEA/DSM/DAPNIA, Service d'Astrophysique (URA 2052 associée au CNRS), Centre d'Etudes de Saclay, F-91191 Gif-sur-Yvette Cedex, France.

Forbes & Priest 1995). By running resistive simulations, it was also proved in Forbes (1991) and Inhester, Birn, & Hesse (1992) that a plasmoid gets formed and that the process exhibits an impulsive phase. There is, however, one strong limitation inherent to all these two-dimensional studies: the produced flux rope is not anchored in the boundary. Then the necessity of performing three-dimensional calculations was strongly underlined (Priest & Forbes 2001).

Three-dimensional approaches have been mainly concerned with the effects of a shear applied to the footpoints of an initial bipolar magnetic configuration. To avoid flux pileup on the walls of the computational box, it proved necessary to give a twisting component to these motions (Amari et al. 1996b; Tokman & Bellan 2002). However, this had the bad effect of limiting the amount of shear along the neutral line, which turned out to be not as strong and coherent as in the axisymmetric case (Hagyard 1990). Consequently, it was noted (Amari et al. 1996b) that some of the field lines may lean sideways, letting the inner flux rope merge through them and limiting below the amount of current associated with the current sheet that would form in two dimensions. A transition toward partial opening was obtained, but without strong dissipation and ejection of a plasmoid.

The effect of converging boundary motions has not been considered yet, and it is the aim of this paper to investigate their possible effects on a bipolar configuration (complex topology fields will not be introduced here) initially in a force-free state and having nonzero helicity contents. In the solar corona, such configurations may be the result of several different processes. They may be associated with a newly emerging active region bringing electric current with it (Leka et al. 1996), or they may be the remnant of post-eruptive arcades that have not relaxed to a potential state. (According to Taylor's classical conjecture, it could be supposed that the field relaxes to a constant- $\alpha$  force-free configuration after an eruptive event. Recently, however, the validity of this idea has been seriously challenged. It has been found indeed to be incorrect in numerical MHD simulations of coronal disruption [Amari & Luciani 2000] and in an analysis of the global budget of an observed flaring active region ejecting at infinity in a magnetic cloud some amount of helicity [Bleybel et al. 2002]). However, the details of these processes, as well as the mechanisms that could lead to the formation in the magnetic structure of a prominence by condensation of cold material, are of no concern to us here.

For our purpose, we first construct numerically in the half-space  $\Omega = \{z > 0\}$  (or more exactly in a cubic box of very large size) a series of initial force-free configurations with the adequate structure. Next, we impose on the boundary  $\{z = 0\}$  some motions converging toward the inversion line, and we determine the resulting evolution of each of our initial configurations by solving the full set of MHD equations. Some of the important questions that we may answer that way are as follows: (1) Do the converging motions contribute to the helicity contents of the magnetic structure? (2) How long can the field evolve quietly in an approximately quasi-static way? (3) What happens when the quiet phase ends, is there production of a twisted flux rope in equilibrium, or is the system subject immediately to a global disruption?

The paper is organized as follows: First, we present some general analytical results. We recall in § 2 (after a description of our model) some properties of two basic physical quantities, the magnetic energy and the relative magnetic helicity, and we derive in § 3 some new formulae governing

their evolution in a quasi-ideal situation. We consider in § 4 a simple exact solution describing, in the quasi-static framework, the evolution of a force-free field driven by a special class of boundary converging motions. The second and main part of the paper is devoted to a description of the results of our numerical simulations. The initial force-free states are constructed in § 5, and their evolution driven by converging boundary motions is considered in § 6. Finally, we discuss the significance of our results, in particular their relevance to a theory of CME, in the concluding § 7.

## 2. MODEL PROBLEM: A CLASS OF INITIAL BOUNDARY VALUE PROBLEMS

This section is devoted to a short description of our model and to a reminder of some basic properties of the magnetic energy and the relative magnetic helicity.

### 2.1. Description of the Model

In the model we consider in this paper, the corona and the photosphere are represented by the half-space  $\Omega = \{z > 0\}$  and the plane  $S = \{z = 0\}$ , respectively.  $\Omega$  is assumed to be filled up with a low- $\beta$  slightly resistive and viscous plasma embedded in a magnetic field  $\mathbf{B}(\mathbf{r}, t)$ . At some initial time  $t_0$ , the field  $\mathbf{B}_0(\mathbf{r}) = \mathbf{B}(\mathbf{r}, t_0)$  is taken to be force-free and to have a finite energy  $W(t_0)$  and a finite magnetic relative helicity  $H(t_0)$ . Therefore, it does obey the equations

$$\nabla \times \mathbf{B}_0 = \alpha_0 \mathbf{B}_0, \quad (1)$$

$$\nabla \cdot \mathbf{B}_0 = 0, \quad (2)$$

with  $\alpha_0(\mathbf{r})$  satisfying the well-known constraint

$$\mathbf{B}_0 \cdot \nabla \alpha_0 = 0. \quad (3)$$

In practice, this initial force-free field can be obtained by several different procedures. Hereafter we shall use a numerical twist and relaxation method, but we could also construct  $\mathbf{B}_0$  by solving a boundary value problem (BVP) in which the normal component  $B_z$  and the function  $\alpha$  are specified, respectively, on the whole boundary  $S$ , and on that part  $S^+$  of  $S$  where  $B_z > 0$  as in Sakurai (1981) and Amari, Boulmezaoud, & Mikic (1999a). Although no mathematical existence theorem has yet been proven for this problem, it seems quite likely that it has always a solution, at least if  $\alpha$  is chosen not too large. Indeed, the existence of solutions has been now established for the similar problem set: either (1) in a bounded domain (Boulmezaoud & Amari 2000), this result being directly relevant in the situation actually considered in our numerics, which are done not in  $\Omega$ , but in a cube  $\Omega_h$ ; or (2) in an unbounded one of the "exterior type," like the exterior of a sphere (Kaiser, Neudert, & von Wahl 2000).

This initial configuration being given, we start imposing for  $t \geq t_0$  some slow motions to its footpoints on the boundary  $S$ , and the field is thus driven into an evolution. These motions are parallel to the surface, i.e., plasma is not allowed to go through  $S$ , and the given velocity  $\mathbf{v}(x, y, 0, t)$  thus satisfies

$$v_z(x, y, 0, t) = 0. \quad (4)$$

Of course, our aim is to determine the evolution of the system, i.e., to compute the field  $\mathbf{B}(\mathbf{r}, t)$ , and we shall do that by solving the full set of equations of magnetohydrodynamics.

### 2.2. Magnetic Energy

The magnetic energy of the field at time  $t$  is defined by

$$W(t) = \frac{1}{8\pi} \int_{\Omega} B^2(t) dv. \quad (5)$$

This quantity bears some interesting relationships with the energies of two auxiliary fields that play an important role in all the evolutionary problems of the type considered in this paper: the potential field  $B_{\pi}(t)$  and the open field  $B_{\sigma}(t)$ , which are uniquely defined by imposing at time  $t$  the boundary conditions

$$B_{\pi z}(x, y, 0, t) = B_{\sigma z}(x, y, 0, t) = B_z(x, y, 0, t) \quad (6)$$

and an asymptotic decay at infinity. These fields have energies given, respectively, by the standard relations

$$W_{\pi}(t) = \frac{1}{16\pi^2} \int_{S \times S} \frac{B_z(x, y, 0, t) B_z(x', y', 0, t)}{|r - r'|} ds ds', \quad (7)$$

$$W_{\sigma}(t) = \frac{1}{16\pi^2} \int_{S \times S} \frac{|B_z(x, y, 0, t) B_z(x', y', 0, t)|}{|r - r'|} ds ds'. \quad (8)$$

As it is well known, the energy  $W(t)$  always satisfies

$$W_{\pi}(t) \leq W(t). \quad (9)$$

Moreover, it is expected on the basis of quite general arguments (Aly 1984, 1991; Sturrock 1991) that

$$W(t_0) \leq W_{\sigma}(t_0), \quad (10)$$

this inequality staying actually valid for  $t \geq t_0$  as long as the field  $B(t)$  approximately evolves in a quasi-static way through a sequence of force-free configurations.

### 2.3. Magnetic Helicity

In the calculations below, we shall follow in particular the evolution of the relative magnetic helicity  $H(t)$ . Then we recall here the definition of that important quantity (Berger & Field 1984). We first introduce the representations

$$B = \nabla \times A \quad (11)$$

and

$$B_{\pi} = \nabla \times A_{\pi} = \nabla V_{\pi} \quad (12)$$

of  $B$  and  $B_{\pi}$  in terms of the potential vectors  $A(t)$  and  $A_{\pi}(t)$  and the scalar potential  $V_{\pi}(t)$ .

Using the gauge arbitrariness of  $A$  and  $A_{\pi}$ , we can choose these quantities in such a way that, at any time  $t$ ,

$$\nabla \cdot A = \nabla \cdot A_{\pi} = 0 \quad \text{in } \Omega, \quad (13)$$

$$A_s = A_{\pi s} \quad \text{on } S, \quad (14)$$

$$\nabla_s \cdot A_s = \nabla_s \cdot A_{\pi s} = 0 \quad \text{on } S, \quad (15)$$

where  $X_s$  denotes quite generally the component of  $X(x, y, 0, t)$  parallel to the boundary  $S$  and  $\nabla_s = \partial_x \hat{x} + \partial_y \hat{y}$ . The compatibility of these conditions is easily verified. We just note that imposing equation (14) is possible because of equation (6). From equations (13) and (15), we get

$$\begin{aligned} -\nabla^2 A_{\pi z} &= [\nabla \times (\nabla \times A_{\pi}) - \nabla(\nabla \cdot A_{\pi})] \cdot \hat{z} \\ &= (\nabla \times B_{\pi}) \cdot \hat{z} = 0 \end{aligned} \quad (16)$$

and

$$\frac{\partial A_z}{\partial z} = \frac{\partial A_{\pi z}}{\partial z} = 0. \quad (17)$$

Therefore,  $A_{\pi z}$  is a harmonic function that satisfies a homogeneous Neumann boundary condition on  $S$  and vanishes at infinity, which implies

$$A_{\pi z} = 0 \quad \text{in } \Omega. \quad (18)$$

Moreover, we can deduce from equations (14) and (15) that there does exist a potential  $\chi(x, y, t)$  such that

$$A_s = A_{\pi s} = \nabla_s \chi \times \hat{z} \quad \text{on } S \quad (19)$$

and

$$B_z = -\nabla_s^2 \chi \quad \text{on } S. \quad (20)$$

With the gauges fixed as above, the relative helicity is given by

$$H = \int_{\Omega} (A \cdot B - A_{\pi} \cdot B_{\pi}) dv. \quad (21)$$

Before closing this subsection, we add one remark of mathematical character. We would like to stress that a rigorous theory of the vector potential in the half-space  $\Omega$  has been recently worked out in Boulmezaoud (1999). Boulmezaoud defines for any real  $\gamma$  the weighted space [with weight function  $\rho(r)$ ]

$$H_{\gamma}(\text{div}; \Omega) = \left\{ v \in \left[ \frac{\mathcal{D}'(\Omega)}{\rho^{\gamma}(r)v} \right]^3 \in [L^2(\Omega)]^3, \rho^{\gamma+1}(r) \nabla \cdot v \in [L^2(\Omega)]^3 \right\}, \quad (22)$$

which is a Hilbert space for the norm

$$\|v\|_{H_{\gamma}(\text{div}; \Omega)} = \left[ \|\rho^{\gamma}(r)v\|_{0, \Omega}^2 + \|\rho^{\gamma+1}(r) \nabla \cdot v\|_{0, \Omega}^2 \right]^{1/2}, \quad (23)$$

and shows the existence of  $A \in [W_{m+1}^m(\Omega)]^3$  ( $m$  an integer) satisfying  $\nabla \cdot A = 0$  in  $\Omega$ , if either  $B \in [W_{m+1}^m(\Omega)]^3$ , with  $m \geq 0$ , or  $B \in H_1(\text{div}; \Omega)$ , with  $m \geq 1$ .

## 3. EVOLUTION OF THE MAGNETIC HELICITY AND THE MAGNETIC ENERGY

We now establish some general formulae for the time variations of the magnetic energy and the magnetic helicity, assuming that we are in a phase of evolution where dissipative processes (either resistive or viscous) can be neglected.

### 3.1. The Tangential Electric Field on $S$

With resistive effects negligible on  $S$  and boundary motions satisfying equation (4), we have from Ohm's law

$$-c \hat{z} \times E_s = \hat{z} \times (v \times B)_s = B_z v_s \quad \text{on } S. \quad (24)$$

By a well-known theorem, the quantity on the right-hand side of the latter relation can be decomposed into an irrotational part and a solenoidal one (Helmholtz's decomposition of a two-dimensional vector). More precisely, there do exist two functions  $f(x, y, t)$  and  $g(x, y, t)$  such that

$$B_z v_s = \nabla_s f + \nabla_s g \times \hat{z}. \quad (25)$$

Here  $f$  and  $g$  need to satisfy the equations

$$\nabla_s^2 f = \nabla_s \cdot (B_z \mathbf{v}_s), \quad (26)$$

$$\nabla_s^2 g = -[\nabla_s \times (B_z \mathbf{v}_s)] \cdot \hat{\mathbf{z}}, \quad (27)$$

obtained by taking successively the surface divergence and rotational of equation (25), and they are uniquely determined if we impose in addition that they do decay to 0 at infinity on  $S$ .

Using Faraday's induction law, we also have

$$\frac{\partial B_z}{\partial t} = -c \nabla \cdot (\mathbf{E}_s \times \hat{\mathbf{z}}) = -\nabla \cdot (B_z \mathbf{v}_s) = -\nabla_s^2 f, \quad (28)$$

and we obtain by comparing this relation with equation (20)

$$f = \frac{\partial \chi}{\partial t}. \quad (29)$$

### 3.2. Magnetic Energy

The evolution of the magnetic energy of the configuration is given by the flux of the Poynting vector through the boundary  $S$ , i.e.,

$$\dot{W} = \frac{c}{4\pi} \int_S (\mathbf{E}_s \times \mathbf{B}_s) \cdot \hat{\mathbf{z}} ds. \quad (30)$$

This relation can be given several equivalent forms by using the relations of the previous subsection. First, we get with the help of equation (24)

$$\dot{W} = -\frac{1}{4\pi} \int_S (\mathbf{v}_s \cdot \mathbf{B}_s) B_z ds. \quad (31)$$

Next, we use the decomposition given by equation (25) in the latter relation, which leads to

$$\begin{aligned} \dot{W} &= -\frac{1}{4\pi} \int_S \mathbf{B}_s \cdot (\nabla_s f + \nabla_s g \times \hat{\mathbf{z}}) ds \\ &= -\frac{1}{4\pi} \int_S [\nabla_s \cdot (f \mathbf{B}_s + g \hat{\mathbf{z}} \times \mathbf{B}_s) - f \nabla_s \cdot \mathbf{B}_s \\ &\quad + g \hat{\mathbf{z}} \cdot \nabla_s \times \mathbf{B}_s] ds \\ &= -\frac{1}{4\pi} \int_S f \partial_z B_z ds - \frac{1}{c} \int_S g j_z ds. \end{aligned} \quad (32)$$

Here we have effected an integration by parts and used Gauss's theorem on  $S$ , equation (2), and Ampere's law

$$\nabla \times \mathbf{B} = \frac{4\pi}{c} \mathbf{j}, \quad (33)$$

where  $\mathbf{j}$  is the electric current density. In equation (32),  $\dot{W}$  appears to be divided into two terms: one related to  $f$  and then to the change of  $B_z$ , and another one related to  $g$  and then to the rotational part of  $B_z \mathbf{v}_s$ .

In the case in which the boundary motions keep  $B_z$  invariant ( $f = 0$ ) and the field in  $\Omega$  is force-free ( $4\pi \mathbf{j}_z = \alpha c B_z$ ), equation (32) reduces to

$$\dot{W} = -\frac{1}{4\pi} \int_S g \alpha B_z ds, \quad (34)$$

a formula that was derived for the first time in Aly (1991).

### 3.3. Magnetic Helicity

The variation of the relative helicity in an arbitrary domain  $D$  is given by (Berger & Field 1984)

$$\dot{H} = 2 \int_{\partial D} (c \mathbf{A}_{\pi s} \times \mathbf{E}_s - \partial_t V_{\pi} \mathbf{A}_{\pi}) \cdot \hat{\mathbf{n}} ds, \quad (35)$$

where  $\hat{\mathbf{n}}$  is the exterior unit normal to the boundary  $\partial D$  of  $D$  and the potential vectors of  $\mathbf{B}$  and  $\mathbf{B}_{\pi}$  are assumed to satisfy the gauge constraints given by equations (13) and (14). With  $D = \Omega$  and the gauge condition given by equation (15) enforced, we have  $\mathbf{A}_{\pi z} = 0$  by equation (18), and the formula above reduces to

$$\dot{H} = -2 \int_S \mathbf{A}_{\pi s} \cdot (c \mathbf{E}_s \times \hat{\mathbf{z}}) ds. \quad (36)$$

Using the representation given by equation (19) for  $\mathbf{A}_{\pi s}$  and equation (24) for  $\mathbf{E}_s$  in the latter equation leads to

$$\dot{H} = -2 \int_S (\nabla_s \chi \times \hat{\mathbf{z}}) \cdot (B_z \mathbf{v}_s) ds, \quad (37)$$

whence, by injecting the decomposition given by equation (25),

$$\begin{aligned} \dot{H} &= -2 \int_S (\nabla_s \chi \times \hat{\mathbf{z}}) \cdot (\nabla_s f + \nabla_s g \times \hat{\mathbf{z}}) ds \\ &= -2 \int_S (\nabla_s f \times \nabla_s \chi) \cdot \hat{\mathbf{z}} ds - 2 \int_S \nabla_s g \cdot \nabla_s \chi ds \\ &= -2 \int_S [\nabla_s \times (f \nabla_s \chi)] \cdot \hat{\mathbf{z}} ds \\ &\quad - 2 \int_S \nabla_s \cdot (g \nabla_s \chi) ds + 2 \int_S g \nabla_s^2 \chi ds. \end{aligned} \quad (38)$$

The first and second integrals on the right-hand side disappear by Stokes and Gauss's theorems, respectively, and the assumed asymptotic decay of the various functions. Therefore, by taking equation (20) into account, we are finally left with the simple expression

$$\dot{H} = -2 \int_S g B_z ds. \quad (39)$$

Of the two functions  $f$  and  $g$ , only  $g$  (which is determined by the rotational part of  $B_z \mathbf{v}_s$ , which does not change  $B_z$ ) appears explicitly in this formula. This does not mean, however, that  $f$  does not play any role: actually, its effect is contained in the time dependence of  $B_z$  given by equation (28).

Another form of equation (39) is obtained by introducing the flow generated by the velocity field  $\mathbf{v}_s$  on  $S$ . If we denote as  $\mathbf{r} = \mathbf{r}(\mathbf{r}_0, t)$  the position at time  $t$  of a material point located at  $\mathbf{r}_0$  at the initial time  $t_0$ , we have  $B_z(\mathbf{r}, t) ds(\mathbf{r}, t) = B_{0z}(\mathbf{r}_0) ds_0(\mathbf{r}_0)$  by flux conservation and then

$$\dot{H} = -2 \int_S g[\mathbf{r}(\mathbf{r}_0, t), t] B_{0z}(\mathbf{r}_0) ds_0. \quad (40)$$

In this form, all the time dependence has been transferred to the function  $g$ , now expressed in terms of Lagrangian coordinates rather than Eulerian ones.

It is worth emphasizing here an important point. The change in the magnetic helicity depends only on quantities ( $B_z$  and  $\mathbf{v}$  on  $S$ ) that are given in our problem as boundary



conditions and not at all on the dynamics of the field  $\mathbf{B}$  inside  $\Omega$ .  $H(t)$  can thus be computed a priori, without having to solve the MHD equations. This makes a striking difference with the energy, whose variation (e.g., eq. [30]) depends on the tangential component of  $\mathbf{B}$  on  $S$ , a quantity that has to be computed a posteriori from the solution  $\mathbf{B}(\mathbf{r}, t)$  in  $\Omega$ .

### 3.4. Symmetric Situations

Let us now consider how the helicity evolves when the boundary conditions satisfy some symmetry conditions. As a first example, let us assume that, like in our numerics reported hereafter,

$$B_z(x, -y, 0, t_0) = -B_z(x, y, 0, t_0), \quad (41)$$

and either

$$v_x(x, -y, 0, t) = -v_x(x, y, 0, t), \quad (42)$$

$$v_y(x, -y, 0, t) = v_y(x, y, 0, t), \quad (43)$$

or

$$v_x(x, -y, 0, t) = v_x(x, y, 0, t), \quad (44)$$

$$v_y(x, -y, 0, t) = -v_y(x, y, 0, t). \quad (45)$$

In the first case, we impose in addition that  $f = 0$ . Then  $B_z$  is time independent on  $S$ , and equation (41) is also satisfied at  $t \geq t_0$ . Using equation (27), we get

$$(gB_z)(x, -y) = (gB_z)(x, y) \quad (46)$$

and

$$\dot{H} = -4 \int_{S^+} gB_z ds \quad (47)$$

( $B_z > 0$  on  $S^+ \subset S$ ). Therefore, we obtain a monotonically increasing (decreasing) helicity if we choose  $g$  to be negative (positive) on  $S^+$ . Equation (47) does apply with a  $\mathbf{v}$  of the vortex type considered in § 5.3. However, it is not valid when  $\mathbf{v}$  is of the purely shearing type  $\mathbf{v} = v(y)\hat{x}$ , with  $v(-y) = -v(y)$ . Such a  $\mathbf{v}$  [used, e.g., in Devore 2000, with  $v(y) = \omega y$ ] leads indeed to a changing  $B_z$  [clearly,  $B_z(x, y, 0, t) = B_z(x, y - v(y)(t - t_0), 0, t_0)$ ].

In the second case (which is that of the converging motions defined in § 3.1), equation (41) is automatically conserved in time. We have

$$(gB_z)(x, -y) = -(gB_z)(x, y) \quad (48)$$

and

$$\dot{H} = 0, \quad (49)$$

i.e., the helicity keeps a constant value.

As a second example, let us consider the case of an axisymmetric field. Then  $f$ ,  $g$ , and  $B_z$  on  $S$  depend only on  $r$ , and  $rB_z = A'$ , with  $A$  the standard flux function. Whence

$$\dot{H} = 2 \int_S \frac{A}{r} g' ds = -2 \int_S \frac{v_\phi}{r} AB_z ds, \quad (50)$$

where we have effected an integration by parts with respect to  $r$  and used equation (25) to evaluate  $g'(r)$ . Then we find (up to a different normalization factor) a relation derived in Aly (1992; his eq. [116]) under the supplementary assumption (not made here)  $v_r = 0$  on  $S$ .

## 4. A SIMPLE ANALYTICAL MODEL

In this section we present a simple analytical model describing the quasi-static evolution of a force-free magnetic field whose footpoints are submitted to a particular class of converging or diverging motions. Comparison of the behaviors of the fields obtained in this model and in the dynamical calculations reported in the next section will lead to some interesting conclusions.

### 4.1. A Sequence of Force-free Fields

Let us choose some continuously differentiable positive function  $\lambda(t)$  satisfying  $\lambda(t_0) = 1$  and define for  $t \geq t_0$  the time sequence of fields

$$\mathbf{B}(\mathbf{r}, t) = \lambda^2(t) \mathbf{B}_0[\lambda(t)\mathbf{r}], \quad (51)$$

where  $\mathbf{B}_0$  is the initial force-free field introduced in § 2.1. The fields  $\mathbf{B}(t)$  are also defined in  $\Omega$ , where they are easily checked to satisfy

$$\nabla \cdot \mathbf{B} = 0, \quad (52)$$

$$\nabla \times \mathbf{B} = \alpha \mathbf{B}, \quad (53)$$

with

$$\alpha(\mathbf{r}, t) = \lambda(t) \alpha_0[\lambda(t)\mathbf{r}]. \quad (54)$$

Then all the fields of the sequence turn out to be force-free magnetic fields. Moreover, if we set

$$\mathbf{v}(\mathbf{r}, t) = -\frac{\dot{\lambda}(t)}{\lambda(t)} \mathbf{r}, \quad (55)$$

$\mathbf{B}$  satisfies the equation of evolution

$$\frac{\partial \mathbf{B}}{\partial t} = \nabla \times (\mathbf{v} \times \mathbf{B}) \quad (56)$$

valid for a field embedded in a perfectly conducting plasma. Therefore, as the velocity  $\mathbf{v}(x, y, 0, t)$  is parallel to  $S$ , it is possible to interpret the sequence as describing a quasi-static evolution of  $\mathbf{B}$  driven by footpoint motions. In particular, we see that imposing  $\lambda(t)$  to be monotonically increasing (decreasing) allows us to describe an evolution driven by motions converging toward (diverging from) the origin  $O$ .

### 4.2. Some Properties of the Sequence

On  $S$ , the normal component of  $\mathbf{B}$  is given by

$$B_z(x, y, 0, t) = \lambda^2(t) B_{0z}[\lambda(t)x, \lambda(t)y, 0], \quad (57)$$

and because of equation (20), we have

$$\chi(\mathbf{r}, t) = \chi[\lambda(t)\mathbf{r}, t_0] = \chi_0[\lambda(t)\mathbf{r}]. \quad (58)$$

Using equation (29), we thus get

$$\begin{aligned} f(\mathbf{r}, t) &= \frac{\partial \chi}{\partial t}(\mathbf{r}, t) = \dot{\lambda}(t) \mathbf{r} \cdot (\nabla_s \chi_0)[\lambda(t)\mathbf{r}] \\ &= \frac{\dot{\lambda}(t)}{\lambda(t)} \mathbf{r} \cdot \frac{\partial \chi}{\partial \mathbf{r}}(\mathbf{r}, t), \end{aligned} \quad (59)$$

or

$$f = \frac{\dot{\lambda}}{\lambda} \mathbf{r} \cdot \frac{\partial \chi}{\partial \mathbf{r}}. \quad (60)$$

Moreover, we have from equation (25)

$$\nabla_s f + \nabla_s g \times \hat{z} = -\frac{\lambda}{\lambda} \mathbf{B}_z \mathbf{r}, \quad (61)$$

whose orthoradial component writes

$$\frac{1}{r} \frac{\partial f}{\partial \phi} - \frac{\partial g}{\partial r} = 0. \quad (62)$$

Along with equation (60), this gives

$$g = \frac{\lambda}{\lambda} \frac{\partial \chi}{\partial \phi}. \quad (63)$$

Both  $f$  and  $g$  can thus be expressed in terms of  $\lambda$  and  $\chi$ , or  $\chi_0$  by using equation (58). Note that we also have from equation (59)

$$\frac{d\chi}{dt} = \frac{\partial \chi}{\partial t} + \mathbf{v} \cdot \nabla_s \chi = 0, \quad (64)$$

i.e.,  $\chi$  is a Lagrangian invariant on  $S$ .

As an immediate consequence of equation (6), the potential field  $\mathbf{B}_\pi(t)$  and the open field  $\mathbf{B}_\sigma(t)$ , which are fully determined by this boundary condition, are given by

$$\mathbf{B}_\pi(\mathbf{r}, t) = \lambda^2(t) \mathbf{B}_\pi[\lambda(t)\mathbf{r}, 0], \quad (65)$$

$$\mathbf{B}_\sigma(\mathbf{r}, t) = \lambda^2(t) \mathbf{B}_\sigma[\lambda(t)\mathbf{r}, 0]. \quad (66)$$

Making a simple change of variable, it is seen at once that the respective energies of  $\mathbf{B}(t)$ ,  $\mathbf{B}_\pi(t)$ , and  $\mathbf{B}_\sigma(t)$  vary according to

$$W(t) = \lambda(t) W(t_0), \quad (67)$$

$$W_\pi(t) = \lambda(t) W_\pi(t_0), \quad (68)$$

$$W_\sigma(t) = \lambda(t) W_\sigma(t_0). \quad (69)$$

All these energies increase (decrease) monotonically if the motions are converging (diverging). Moreover, we have

$$\frac{W(t)}{W(t_0)} = \frac{W_\pi(t)}{W_\pi(t_0)} = \frac{W_\sigma(t)}{W_\sigma(t_0)}, \quad (70)$$

which implies that the energy of the open field cannot be exceeded at some time  $t$  if it is not exceeded at the initial time  $t_0$ . Then the sequence would be useless for someone wanting to disprove the validity of the conjecture quoted in § 2.2, according to which one has always  $W(t) \leq W_\sigma(t)$  when the field is force-free.

Consider now the relative helicity of the fields  $\mathbf{B}(t)$ . Making the obviously possible choices

$$\mathbf{A}(\mathbf{r}, t) = \lambda(t) \mathbf{A}[\lambda(t)\mathbf{r}, t_0], \quad (71)$$

$$\mathbf{A}_\pi(\mathbf{r}, t) = \lambda(t) \mathbf{A}_\pi[\lambda(t)\mathbf{r}, t_0], \quad (72)$$

for the potential vectors of  $\mathbf{B}(t)$  and  $\mathbf{B}_\pi(t)$ , respectively, we obtain

$$H(t) = H(0) \quad (73)$$

(just effect a change of variable in the integral defining  $H$ ). Then the helicity keeps a constant value all along the sequence.

Finally, let us consider the ideal stability properties of the fields  $\mathbf{B}(t)$ . We may test the stability of an equilibrium by applying to it an admissible displacement moving a point

from  $\mathbf{r}_0$  to  $\mathbf{r}(r_0)$  [by admissible, we mean here one-to-one, of Jacobian  $J = D(\mathbf{r})/D(\mathbf{r}_0) > 0$ , and not moving the boundary points at which  $\mathbf{B}_z \neq 0$ ] and by comparing the energy

$$\tilde{W} = \frac{1}{8\pi} \int_{\Omega} \frac{1}{J} |\mathbf{B} \cdot \nabla_0 \mathbf{r}|^2 dv \quad (74)$$

of the deformed field with that of the equilibrium field. Noticing that we may establish a one-to-one correspondence between the deformations  $\mathbf{r}(r_0)$  admissible for  $\mathbf{B}_0$  and those  $\mathbf{r}_t(r_0)$  admissible for  $\mathbf{B}(t)$  by setting

$$\mathbf{r}(r_0) \longleftrightarrow \mathbf{r}_t(r_0) = \frac{1}{\lambda(t)} \mathbf{r}[\lambda(t)\mathbf{r}_0], \quad (75)$$

we get for two deformations associated that way

$$\tilde{W}(t) - W(t) = \lambda(t) [\tilde{W}(0) - W(0)], \quad (76)$$

which shows clearly that  $\mathbf{B}(t)$  has the same stability properties as  $\mathbf{B}(0)$ . If the latter is stable (unstable), so is  $\mathbf{B}(t)$ . Note that we have not supposed the displacements  $|\mathbf{r}(r_0) - \mathbf{r}_0|$  to be arbitrarily small, and then stability may be understood in the statement above as being either linear or nonlinear. In particular, we can claim the following result. Suppose that we start from a force-free field  $\mathbf{B}(0)$  that is unconditionally nonlinearly stable (i.e., it is an absolute minimum energy state among all the configurations that can be obtained from it by an ideal finite deformation): then  $\mathbf{B}(t)$  has the same property.

As far as the specific problem considered in this paper is concerned, we can essentially retain the following statement from the considerations above: from an initial force-free state  $\mathbf{B}_0$  and a monotonically increasing function  $\lambda(t)$  satisfying  $\lambda(t_0) = 1$ , it is possible to construct a time sequence of force-free configurations  $\mathbf{B}(t)$  such that (1)  $\mathbf{B}(t)$  describes an ideal quasi-static evolution starting from  $\mathbf{B}(t_0) = \mathbf{B}_0$  and driven by converging boundary motions on  $S$ , (2) all the fields  $\mathbf{B}(t)$  are as (ideally) stable as  $\mathbf{B}_0$ , (3) the relative helicity of  $\mathbf{B}(t)$  is equal to that of  $\mathbf{B}_0$ , and (4) the energy of  $\mathbf{B}(t)$  increases monotonically in time.

## 5. CONSTRUCTION OF A NONZERO RELATIVE HELICITY FORCE-FREE CONFIGURATION $\mathbf{B}_0$

We now start presenting our numerical simulations, which are done by substituting to the half-space  $\Omega$  a cubic box  $\Omega_h$  of large size (compared to the characteristic scale of our boundary conditions). As a first step, we construct in this section a series of initial force-free states  $\mathbf{B}_0$ . For that, we set up at time  $t = 0$  a potential field, which we submit to twisting boundary motions for  $t \in [0, t_s]$  and to a viscous relaxation, with no boundary motions, for  $t \in [t_s, t_0]$ .

### 5.1. Initial Potential Configuration

Our initial potential magnetic field

$$\mathbf{B}_\pi(x, y, z, 0) = \nabla V_\pi(x, y, z, 0) \quad (77)$$

is computed by solving the following mixed (Neumann-Dirichlet) BVP for the scalar potential  $V_\pi \in W_{m+k}^{m+1}(\Omega_h)$ ,

$m \geq 1$  an integer:

$$\nabla^2 V_\pi = 0 \quad \text{in } \Omega_h, \quad (78)$$

$$\frac{\partial V_\pi}{\partial z} = \xi(x, y) \quad \text{for } z = 0, \quad (79)$$

$$V_\pi = \zeta \quad \text{on } \partial\Omega_h \setminus \{z = 0\}, \quad (80)$$

where  $\xi$  represents the given distribution of  $B_z$  on  $\{z = 0\}$  and

$$\zeta(\mathbf{r}) = -\frac{1}{2\pi} \int_S \frac{\xi(\mathbf{r}')}{|\mathbf{r} - \mathbf{r}'|} ds' \quad (81)$$

is the value that would be taken by  $V_\pi$  on the boundary of the box ( $z \neq 0$ ) if the calculation was done in the whole  $\Omega$ .

Here we take

$$\xi(x, y) = \sum_{k=1}^N a_k^+ e^{\Gamma_k^+(x, y)} + a_k^- e^{\Gamma_k^-(x, y)}, \quad (82)$$

with

$$\Gamma_k^\pm(x, y) = -\frac{(x - x_{ck}^\pm)^2}{\sigma_x^\pm} - \frac{(y - y_{ck}^\pm)^2}{\sigma_y^\pm}. \quad (83)$$

Although this distribution of flux does not have a compact support, it is clearly decreasing fast enough in  $\mathbb{R}^2$  for equation (81) to be applied. As for the values of the parameters, we choose  $\Omega_h = [-20, 20] \times [-20, 20] \times [0, 40]$  for our computational domain and set  $N = 1$ ,  $\sigma_x^\pm = 2$ ;  $\sigma_y^\pm = 1$ ,  $a_k^+ = -a_k^- = 1$ ; and  $x_{c1}^+ = x_{c1}^- = 0$ ,  $y_{c1}^+ = -y_{c1}^- = 0.8$ . As shown in Figure 1, the field  $\mathbf{B}_\pi$  constructed that way mimics an arcade-like structure in the upper half-space  $\Omega$ . Note that  $\mathbf{B}_\pi$  represents a good numerical equilibrium (electric current and magnetic forces are numerically small), since it has been constructed as the solution of a BVP on our computational mesh rather than by effecting a viscous relaxation as in Amari et al. (1996b).

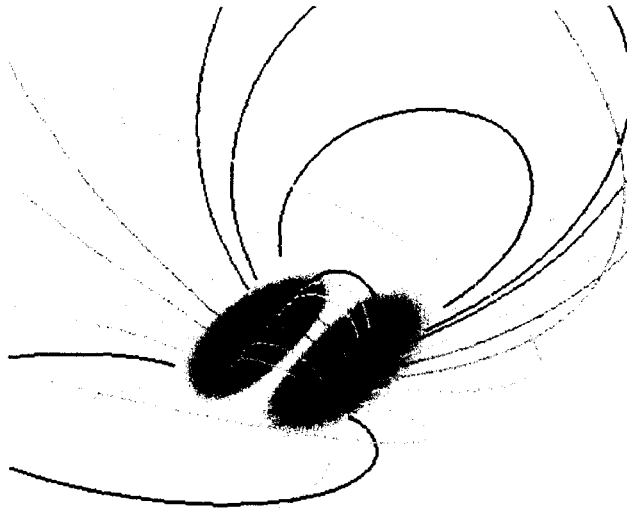


FIG. 1.—Selected field lines of the initial bipolar potential magnetic configuration. [See the electronic edition of the Journal for a color version of this figure.]

## 5.2. MHD Equations

Before describing the deformation of  $\mathbf{B}_\pi$  into a nonlinear force-free state at  $t_0$ , let us write the system of the MHD equations we shall use. In nondimensionalized form, it is given by (Amari et al. 1996b; Amari, Luciani, & Joly 1999b)

$$\rho \frac{\partial \mathbf{v}}{\partial t} = -\rho(\mathbf{v} \cdot \nabla \mathbf{v}) + (\nabla \times \mathbf{B}) \times \mathbf{B} - \nabla p + \nabla \cdot (\nu \rho \nabla \mathbf{v}) + \rho \mathbf{g}, \quad (84)$$

$$\frac{\partial \mathbf{B}}{\partial t} = \nabla \times (\mathbf{v} \times \mathbf{B}) - \nabla \times (\eta \mathbf{j}), \quad (85)$$

$$\frac{\partial \rho}{\partial t} = -\nabla \cdot (\rho \mathbf{v}), \quad (86)$$

$$\frac{\partial p}{\partial t} = -\mathbf{v} \cdot \nabla p - \Gamma p (\nabla \cdot \mathbf{v}) + H, \quad (87)$$

$$\mathbf{j} = \nabla \times \mathbf{B}, \quad (88)$$

$$\nabla \cdot \mathbf{B} = 0, \quad (89)$$

where  $\rho$ ,  $\nu$ ,  $\eta$ , and  $\Gamma$  are the mass density, the kinematic viscosity, the resistivity, and the adiabatic index of the plasma, respectively.

Small values are used in this paper for the dissipation coefficients:  $\nu = 10^{-2}$  to  $10^{-3}$  for the kinematic viscosity and  $\eta = 10^{-4}$ ,  $10^{-5}$ , 0 for the resistivity (for our mesh resolution, this gives Lundquist numbers of order  $10^4$ ,  $10^5$ ), which allows us to neglect the term  $H$  in equation (87). The plasma  $\beta$  is taken to be  $10^{-3}$  (i.e., of the order of the very small values observed in the corona) or 0, without any differences being actually found between the results. When we choose  $\beta = 0$ , we need to fix arbitrarily a mass density profile and of course neglect the gravity term in equation (84). Here we choose  $\rho = B^2$ , which ensures a constant Alfvén velocity, or  $\rho = 1$ . Alternative choices of density profiles (exhibiting, for instance, a slower decrease with distance) have been found not to lead to sensibly different results.

The MHD equations are discretized on a nonuniform mesh ( $141 \times 121 \times 91$  nodes) and solved by using our semi-implicit scheme (Amari et al. 1999b).

## 5.3. Twisting Evolution: $f = 0$

For  $t \geq 0$ , we impose a twisting velocity field to the footpoints at the bottom of the box. The velocity field is prescribed by choosing in equation (25)

$$\mathbf{f} = 0 \quad (90)$$

(therefore the distribution of  $B_z$  is preserved for  $z = 0$ ), and to allow comparison with our previous calculations, we use as in Amari et al. (1996b) the velocity field  $\mathbf{v}_s = \nabla_s \phi \times \hat{\mathbf{z}}$ , with

$$\phi = \phi(B_z, t) = v_0 R(t) B_z^2 e^{-[(B_z^2 - B_{z,\max}^2)/B_{z,\max}]}, \quad (91)$$

where  $B_{z,\max} = \sup_S \xi$  and  $v_0 = 10^{-2}$  (then  $v_0$  is small compared to the Alfvén speed  $v_A = 1$ ).  $R$  is a ramp function that is used to smoothly switch on or off the velocity field. It is chosen to be linear, the maximum velocity  $10^{-2}$  being reached at  $t = 10\tau_A$ . This velocity field corresponds to two parallel vortices rotating in the same direction, as in Amari et al. (1996b). It is shown in Figure 2. Although an explicit formula for  $g$  is not given, it appears clearly that one may solve equation (27) for the unique solution  $g$ , which we will

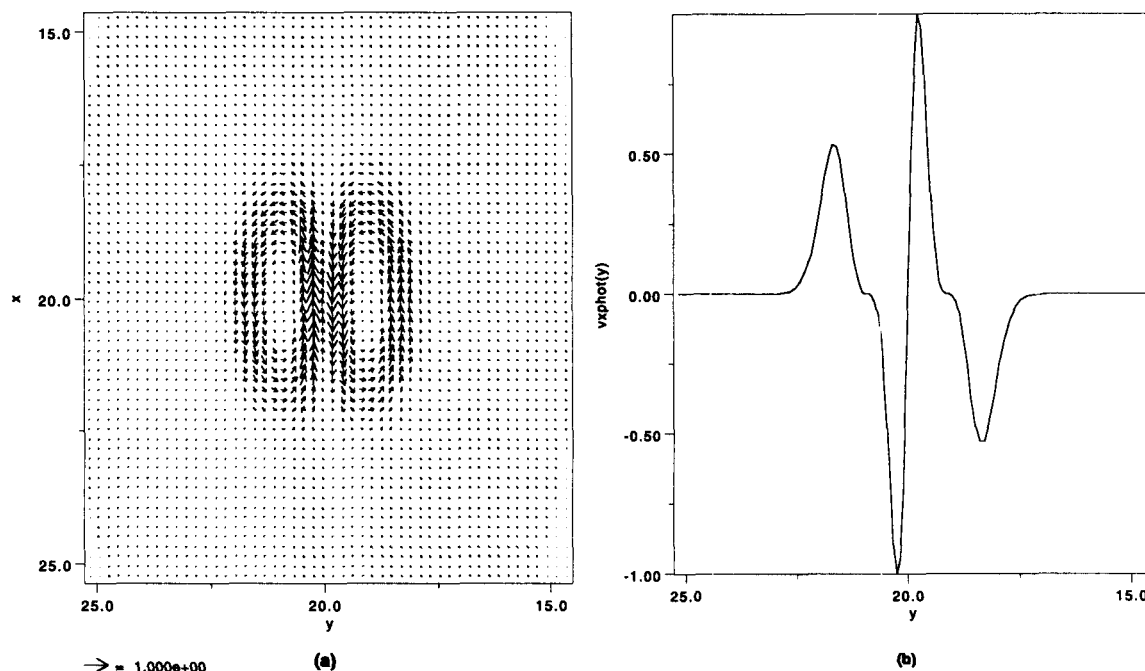


FIG. 2.—(a) Vector plot and (b) cut at  $\{x = 0\}$  of the twisting boundary flow applied to the footpoints of the field lines of the initial configuration shown in Fig. 1 used to construct a nonzero helicity force-free field.

nevertheless not need to use explicitly in what follows. Since from the definition of  $g$  one may deduce  $g'(B_z) = B_z \phi'(B_z)$ , one may easily check that the parity conditions of equation (46) for  $g$  are fulfilled. On the other faces of the box, we take the homogeneous Dirichlet condition  $v = 0$  as in Amari et al. (1996b), which is the adequate condition for a viscous plasma in contact with a nonmoving wall. The viscosity is fixed to  $10^{-3}$  and the uniform resistivity vanishes ( $\eta = 0$ ).

The photospheric twisting motions are applied from  $t = 0$  to  $t = t_s$  (with these times being expressed in units of  $\tau_A$ ). By giving to  $t_s$  different values (here  $t_s = \{0, 50, 100, 200, 400\}$ ), it is possible to generate a series of states  $U^{t_s} = (B^{t_s}, v^{t_s}, \rho^{t_s}, p^{t_s})$  ranging from moderately sheared to highly sheared configurations. We use  $U^0$  as a reference state. As in Amari et al. (1996b), the shearing process brings up shear near the neutral line while twist is introduced as one moves away from the neutral line on  $\{z = 0\}$ . The evolution along this phase is found to be almost quasi-static. The magnetic field acquires an energy that is monotonically increasing (see eq. [32] with  $f = 0$ ) and magnetic helicity. Consistently with equation (47) (we are here in a situation where eqs. [41], [42], and [43] are satisfied), the helicity turns out to be negative, its absolute value increasing monotonically and even at a constant rate after the transient phase during which the ramp is applied. As shown in Figures 3 and 4,  $|H^{t_s}|$  and  $W^{t_s}$  are increasing functions of  $t_s$ .

#### 5.4. Relaxation to an Equilibrium: $f = g = 0$

At  $t = t_s$  the driving photospheric velocity is switched off and the system evolves ideally ( $\eta = 0$ ) through a viscous relaxation procedure that is stopped at  $t = t_0$ , when the field has reached an accessible stable numerical force-free state.

As expected from equations (32) and (39), this phase ( $f = g = 0$ ) implies no injection of magnetic energy and

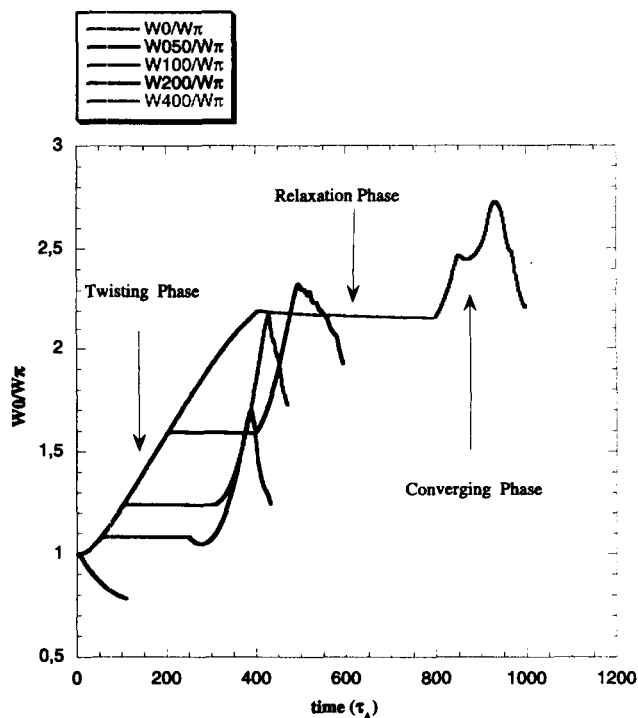


FIG. 3.—Variation of the magnetic energy for various periods during which the twisting boundary flow on Fig. 2 is applied to the potential configuration from  $t = 0$  to  $t = t_s$  and then switched off to reach a relaxed state at  $t = t_0$ , and then converging motions are applied. The various cases  $t_s = 0, 50, 100, 200, 400$  (in units of  $\tau_A$ ) are represented. Magnetic energy  $W$  is expressed in units of  $W_\pi$  (see text). The arrows indicate the three phases for the particular case  $t_s = 400$  in the same units. [See the electronic edition of the Journal for a color version of this figure.]

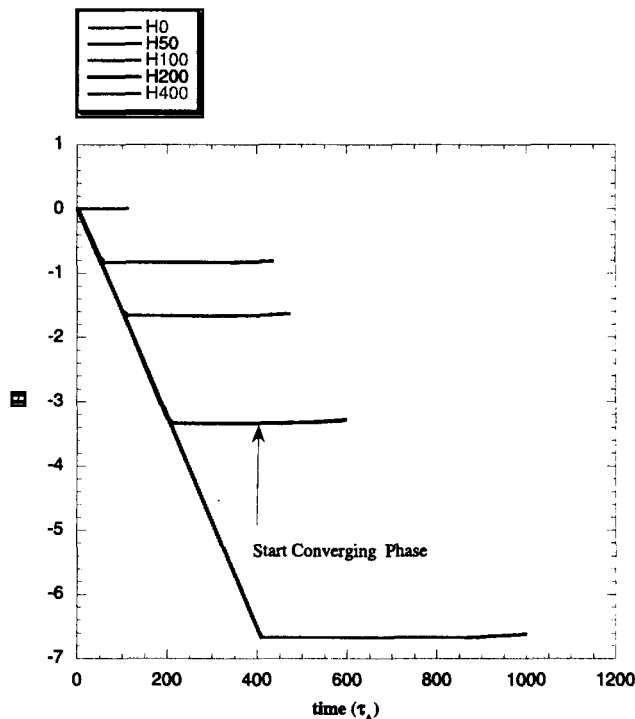


FIG. 4.—Variation of the magnetic helicity for various periods during which the twisting boundary flow on Fig. 2 is applied to the potential configuration from 0 to  $t = t_s$  and then switched off for reaching a relaxed state at  $t = t_0$ , and then converging motions are applied. The various cases  $t_s = 0, 50, 100, 200, 400$  (in units of  $\tau_A$ ) are represented. Magnetic helicity  $H$  represents the relative helicity with our gauge (see text). The arrow indicates the starting beyond which converging motions are applied for the particular case  $t_s = 200$ . [See the electronic edition of the Journal for a color version of this figure.]

helicity. That this is the case indeed is clearly seen in Figures 3 and 4, where these quantities appear to keep constant values for  $t \in [t_s, t_0]$  and for all the values of  $t_s$ , apart from a small variation associated with the linear ramp. Various equilibrium states  $U^i$  with various energy and magnetic helicity levels are thus obtained at  $t = t_0$ .

It is worth noticing that we have chosen, on purpose, the times  $t_s$  small enough in order to not reach the critical threshold beyond which the configuration starts to inflate more rapidly (Amari et al. 1996b). Otherwise, we would not get equilibria at  $t_0$ . Figure 5 shows the equilibrium configurations obtained at  $t_s = 200\tau_A$  and  $t_0 = 400\tau_A$ . We have selected three subsets of field lines to illustrate the effect of the applied velocity field (shear and rotation). The amount of magnetic helicity injected in the initial configuration is clearly not small. We remark in this example that the magnetic energy, although not negligible compared to the potential energy, is still below the energy of the open field  $B_\sigma(t_0)$ , which we found to be  $W_\sigma(t)/W_\pi(0) = 3$  for  $t \leq t_0$  during this phase that preserves  $B_z$ , upon which  $W_\sigma$  depends.

## 6. CONVERGING MOTION-DRIVEN EVOLUTION: $f \neq 0$

We now apply for  $t \geq t_0$  converging motions to the foot-points of the force-free fields  $B_0 = B(t_0)$  constructed in the previous section.

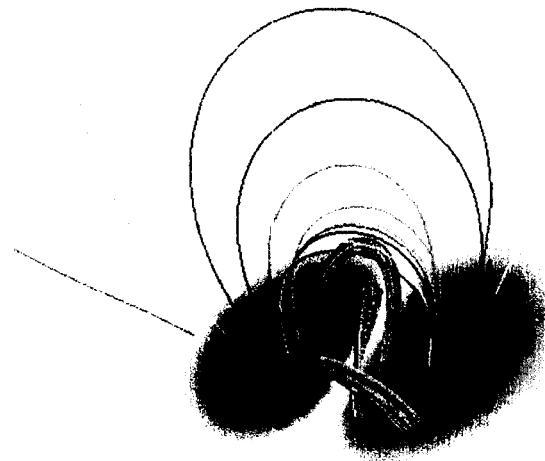


FIG. 5.—Field lines of the magnetic configuration associated with a relaxed equilibrium obtained from the potential configuration shown in Fig. 1 after twisting boundary motions have been applied up to  $t = t_s$  and relaxation up to  $t = t_0$ ; case  $t_s = 400\tau_A$ . Although the configuration is made of a continuum of field lines, only field lines belonging to three flux tubes are shown, as well as outer arcades, so that the effects of central strong shear and outer twist appear. [See the electronic edition of the Journal for a color version of this figure.]

### 6.1. Boundary Motions

Our boundary motions are chosen to converge toward the inversion line  $\{x = 0\}$  at the velocity

$$v_s(x, y) = -B_z(x, y, 0, 0)\hat{y} = -\xi(x, y)\hat{y}, \quad (92)$$

which practically vanishes, as required for consistency, on the boundary of the basis of our box. This velocity is associated with functions  $f$  and  $g$ , which are both nonzero (they do satisfy  $\partial_x f = -\partial_y g$ ), but they can be computed only numerically. A cut of this flow along the axis  $\{x = 0\}$  (Fig. 6) shows that it is continuous and has the typical property of the flows usually introduced in axisymmetric situations.

The resulting evolution is still assumed to be ideal ( $\eta = 0$ ). As shown below, it is characterized by the existence of two qualitatively different phases: a quasi-static phase for  $t_0 \leq t \leq t_c$  and a disruption phase for  $t_c < t$ .

### 6.2. Existence of an Equilibrium Phase

The simulations show the existence of a time  $t_c > t_0$  such that the field evolves quasi-statically through a sequence of force-free equilibria for  $t_0 \leq t \leq t_c$ . Magnetic energy is not monotonically increasing from the beginning of this phase, as shown in Figure 3. For the reference case (corresponding to  $t_s = 0$ ) it is even monotonically decreasing. However, we get  $W(t_c) - W(t_0) > 0$  for all the values of  $t_s \neq 0$ . It is interesting to note that the amount of magnetic energy injected in the configuration during this quiet phase is relatively large compared to the amount that has been stored during

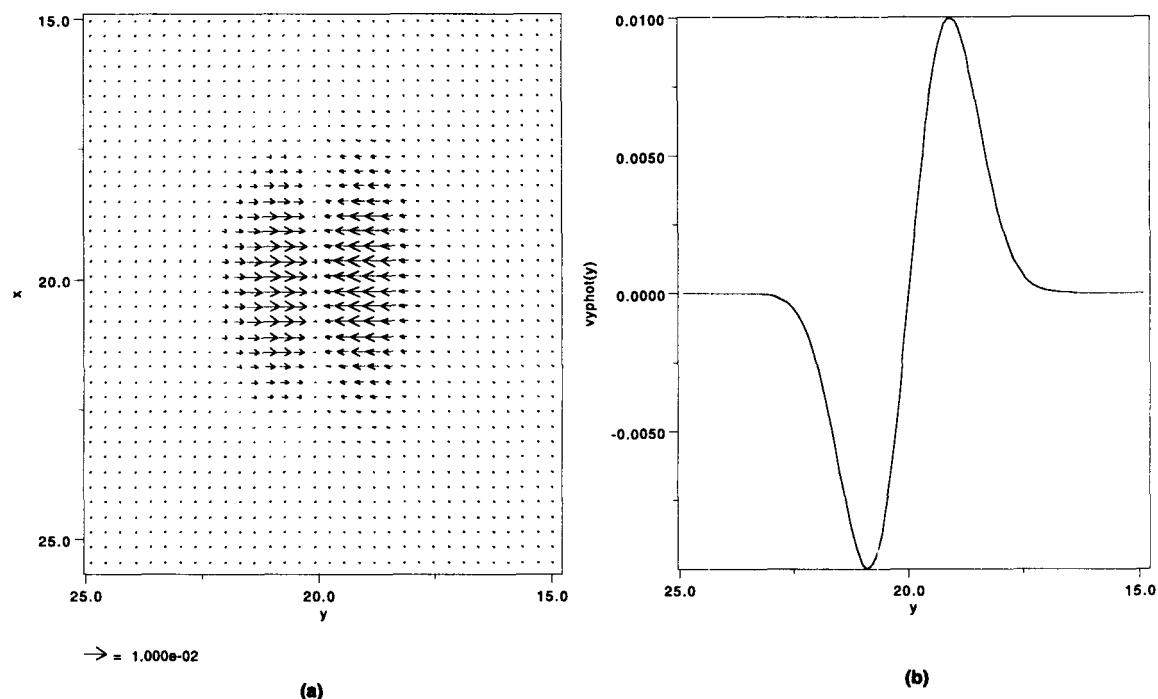


FIG. 6.—(a) Vector plot and (b) cut and variations along the  $y$ -axis (cut at  $\{x = 20\}$ ) of the boundary converging flow applied to the footpoints of the configuration for  $t > t_0$ .

the global shearing-twisting process with  $f = 0$ . However, we still found  $W(t) < W_\sigma(t)$  all along.

Magnetic shear (defined to be the angle between the inversion line and the transverse field) increases continuously, as seen in Figures 7 and 8. The effect of the converging boundary velocity field is to effectively make the field more aligned with the inversion line, but by keeping the topology to be that of a highly sheared arcade core.

Magnetic helicity is almost constant during this phase [i.e.,  $H(t) = H(t_0)$  for  $t_0 \leq t \leq t_c$ ]. This result is fully consistent with equation (49), which applies here as equations (41), (44), and (45) are satisfied. The cases  $U^{50}$  and  $U^{400}$  show dips in the magnetic energy evolution. We checked for  $U^{50}$  that this dip ( $t = 280\tau_A$ ) corresponds effectively to the existence of a neighboring equilibrium as shown in Figure 9, when the driver has been switched off with the linear ramp. This explains the still small rising of magnetic energy, which keeps a constant value, while kinetic energy keeps decreasing. However, we found that the reached equilibrium has still an arcade-like topology with no twisted flux rope. The case of  $U^{400}$ , which will be discussed below, remains in equilibrium in the rising phase (for magnetic energy) that precedes the dip.

### 6.3. Existence of a Disruption Phase

As shown in Figure 3, there exists a  $t_c$  at which the configuration  $U^{t_c}$  experiences a transition toward a dynamic evolution, with a nonnegligible amount of magnetic energy being dissipated [ $W(t) < W(t_c)$ ]. As shown in Figure 10, this transition is associated with a change in the topology of the magnetic field from an arcade-like form to a twisted ropelike form. This structure rises up, reconnecting strongly with the overlying arcade lines, as well as below where new small arcades are observed to reform as shown in Figure 11.

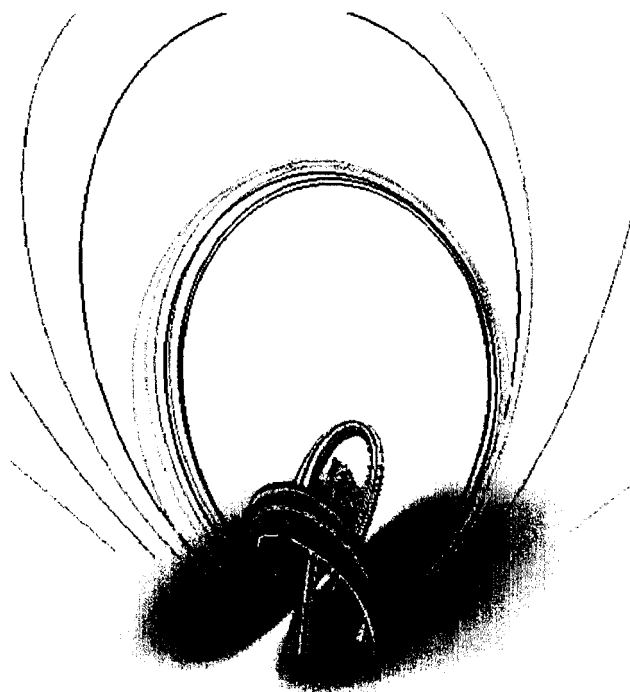


FIG. 7.—Field lines showing the configuration obtained for  $t_s = 200\tau_A$  after a converging velocity field has been applied from  $t_0 = 400\tau_A$  to  $t = 450\tau_A$ . [See the electronic edition of the Journal for a color version of this figure.]

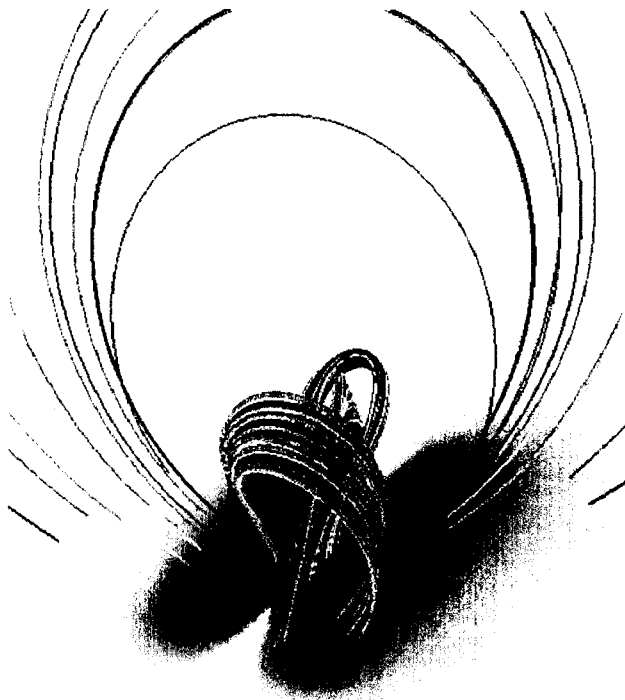


FIG. 8.—Field lines showing the configuration obtained for  $t_s = 200\tau_A$  after a converging velocity field has been applied from  $t_0 = 400\tau_A$  to  $t = 480\tau_A$  (close to the nonequilibrium critical point). [See the electronic edition of the Journal for a color version of this figure.]

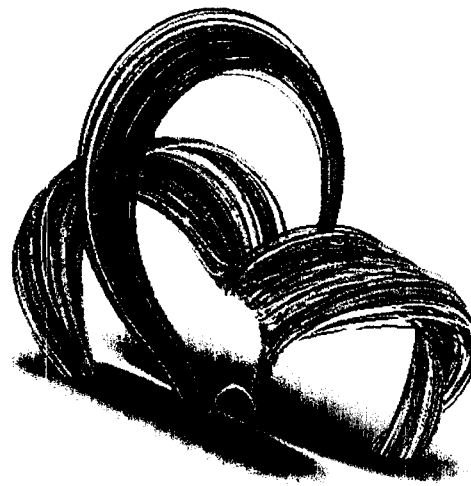


FIG. 10.—Field lines showing the configuration obtained for  $t_s = 200\tau_A$  after a converging velocity field has been applied from  $t_0 = 400\tau_A$  to  $t = 498\tau_A$ . The nonequilibrium critical point has been past, and magnetic reconnection leads to the formation of a three-part structure: twisted flux rope of about  $2\pi$  twist, small new arcades below, and overlaying arcade revealing a plasmoid-like magnetic structure. This structure is, however, far from equilibrium. [See the electronic edition of the Journal for a color version of this figure.]

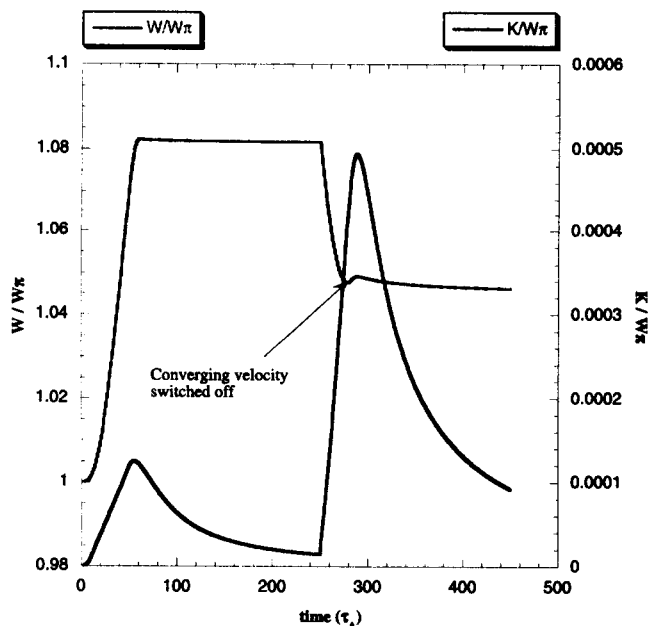


FIG. 9.—Evolution of the magnetic and kinetic energies (in units of  $W_\pi$ ; see text) after the converging boundary velocity field has been switched off (with a linear ramp of  $t = 10\tau_A$ ), in the dip (at  $t = 280\tau_A$ ) of the energy curve of Fig. 3 for the case  $t_s = 50\tau_A$ . The existence of a neighboring equilibrium state is associated with the constant value reached by the magnetic energy while the total kinetic energy keeps decreasing toward zero. [See the electronic edition of the Journal for a color version of this figure.]

A three-part magnetic structure is associated with this state: (1) a twisted flux rope running through (2) a global arcade and above (3) small loops. It is worth noticing that this reconnection going on (with transfer of twist) from the strongly sheared inner field lines toward the outer ones (less sheared) may even lead to a point where the center of the spots (corresponding to infinitely twisted lines) leads to field lines having a high twist. However, this state is not in equilibrium, as we obtain eventually  $v > v_A$  in some region.

As seen in Figure 12, the transverse magnetic field component exhibits a reversal in the sign of  $B_y$  along the inversion line that is compatible with the appearance of the twisted flux rope, while the magnetic configuration remains arcade-like with high magnetic shear prior to the disruption.

For all the cases considered in this study, we found that there is no neighboring equilibrium close to  $U'$  for some  $t > t_c$ . This point is checked by performing a relaxation procedure during which the driving boundary velocity field is switched off. The configuration does not relax toward an equilibrium but still experiences a strong dissipation with acceleration of the plasma. Figure 13 shows the evolution of energies after the velocity has been switched off just after the critical point of disruption  $t_s = 498\tau_A$ . It is worth noticing that the configuration, although far from equilibrium, exhibits a twisted flux rope.

The case  $t_s = 400\tau_A$  shows a first dip in the magnetic energy at  $t = 870\tau_A$ . This dip does not correspond to the existence of a neighboring equilibrium, as shown in Figure 14, where the boundary driver has been switched off

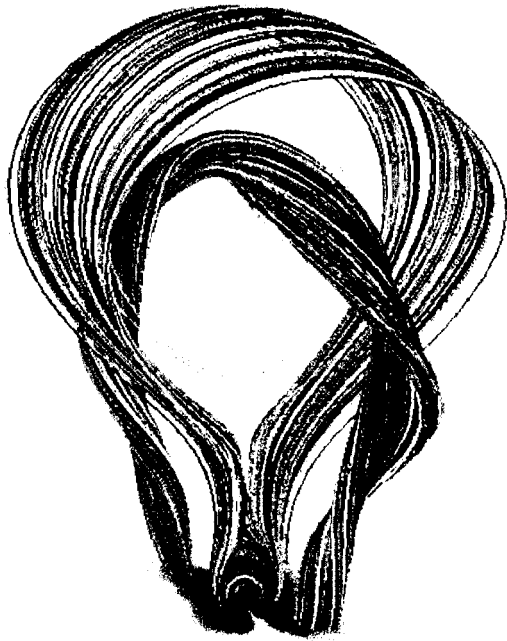


FIG. 11.—Field lines showing the configuration obtained for  $t_s = 200\tau_A$  after a converging velocity field has been applied from  $t_0 = 400\tau_A$  to  $t = 530\tau_A$ . Reconnection goes on with the three-part structure conserved. One field line having a twist greater than  $2\pi$  between the arcade and the flux rope is shown. [See the electronic edition of the *Journal* for a color version of this figure.]

with a linear ramp of  $10\tau_A$ . Magnetic reconnection associated with a disruption occurs with a strong decrease in magnetic energy, while kinetic energy rises strongly before slowly approaching a finite value. We have found that the magnetic topology during this disruption phase exhibits a twisted flux rope. It is worth noticing that unlike the other cases, the rate of decrease of magnetic energy becomes dominated by the injection rate associated with the converging motions when they are present (as shown in Fig. 3), such that a second disruption phase occurs. However, during the second rising phase of magnetic energy, no equilibrium exists while the configuration shows a twisted flux rope far from equilibrium.

It is worth noticing that, although for theoretical reasons we presented cases for which the velocity field is applied all along the evolution, this leads to unrealistic final configurations: at the end the two spots have been so much compressed against each other that they are almost reduced to two straight segments. This extreme limit may explain the small deviations of the magnetic helicity from keeping a constant value. It is interesting to remark that the existence of a critical time beyond which no relaxation toward a neighboring equilibrium exists implies that one does not need to approach this absolute limit.

## 7. DISCUSSION

In this paper we have addressed the problem of the evolution of a three-dimensional magnetic field driven by con-

verging motions imposed on the photosphere  $S$ , with the initial field  $B_0$  being a stable force-free field having a non-zero relative helicity. In a first step, we have considered a simple analytical model describing a situation of that type. In that model, the driving motions are of a quite peculiar type, as all the points of  $S$  suffer at any time  $t$  a homologous contraction toward the origin. The evolving field  $B(t)$  exhibits, however, some interesting features: (1)  $B$  evolves quasi-statically through a sequence of force-free configurations that stay ideally stable and even unconditionally nonlinearly stable if  $B_0$  itself has this property, (2) the magnetic energy increases monotonically in time, and (3) the helicity keeps its initial value. This suggests that the system can suffer a disruption only if reconnection is allowed by a nonzero resistivity of the plasma. It is worth noticing that this simple analytical model may also be relevant to the divergence of a magnetic structure from the center of a supergranulation cell toward its borders, a characteristic picture of the quiet Sun.

Next, we have reported the results of extensive numerical simulations. After having constructed a series of initial stable force-free fields  $B_0 = B(t_0)$ , with  $|H(t_0)| > 0$  and still the initial  $B_z$  on  $S$ , by deforming a given potential field in a two-step (twisting+relaxation) process, we have evolved these  $B_0$  by imposing on  $S$  motions converging toward their straight polarity inversion line. In all the cases we have considered (either with small or large helicity), the evolution of the field exhibits two different phases. In the first one, the evolution is almost quasi-static. The magnetic topology remains arcade-like, with a shear along the inversion line increasing, magnetic energy being stored, and helicity keeping its initial value. The evolution in this phase is thus at least qualitatively quite similar to the one shown by the solution of the analytical model introduced above. At some critical stage, however, this quiet phase is stopped and the configuration experiences a transition to a second dynamic and strongly dissipative phase, during which reconnection leads to the formation of a twisted flux rope, however not in equilibrium.

For defining the velocity field on the boundary (either during the twisting phase allowing to construct the initial field or during the converging phase), we have used a two-dimensional Helmholtz's representation of  $B_z v_s$  (or equivalently of the tangential electric field) on  $S$ , in which appear two scalar functions  $f$  and  $g$ . We have derived new formulae for the variation of the energy and the helicity in terms of these functions and checked in our calculations that the helicity injection rate was in good accord with that analytically derived. We have also checked that the magnetic energy was, at any time, smaller than the energy of the open field with the same flux distribution on the boundary. The conjecture formulated by Aly (1984) thus appears to be compatible with our calculations.

Our three-dimensional results complete the two-dimensional ones reported earlier (Priest & Forbes 1990; Forbes & Priest 1995; Forbes 1991; Inhester et al. 1992). These authors have shown the existence of a catastrophic nonequilibrium transition, implying the ejection of a plasmoid, when the flux distribution evolves in some adequate way on the boundary. Their conclusions, however, were limited by the existence of an unanchored flux rope and the unknown issue of nonequilibrium in three dimensions. This paper settles these important issues, showing that the system dynamically reconnects as soon as it loses equilibrium,



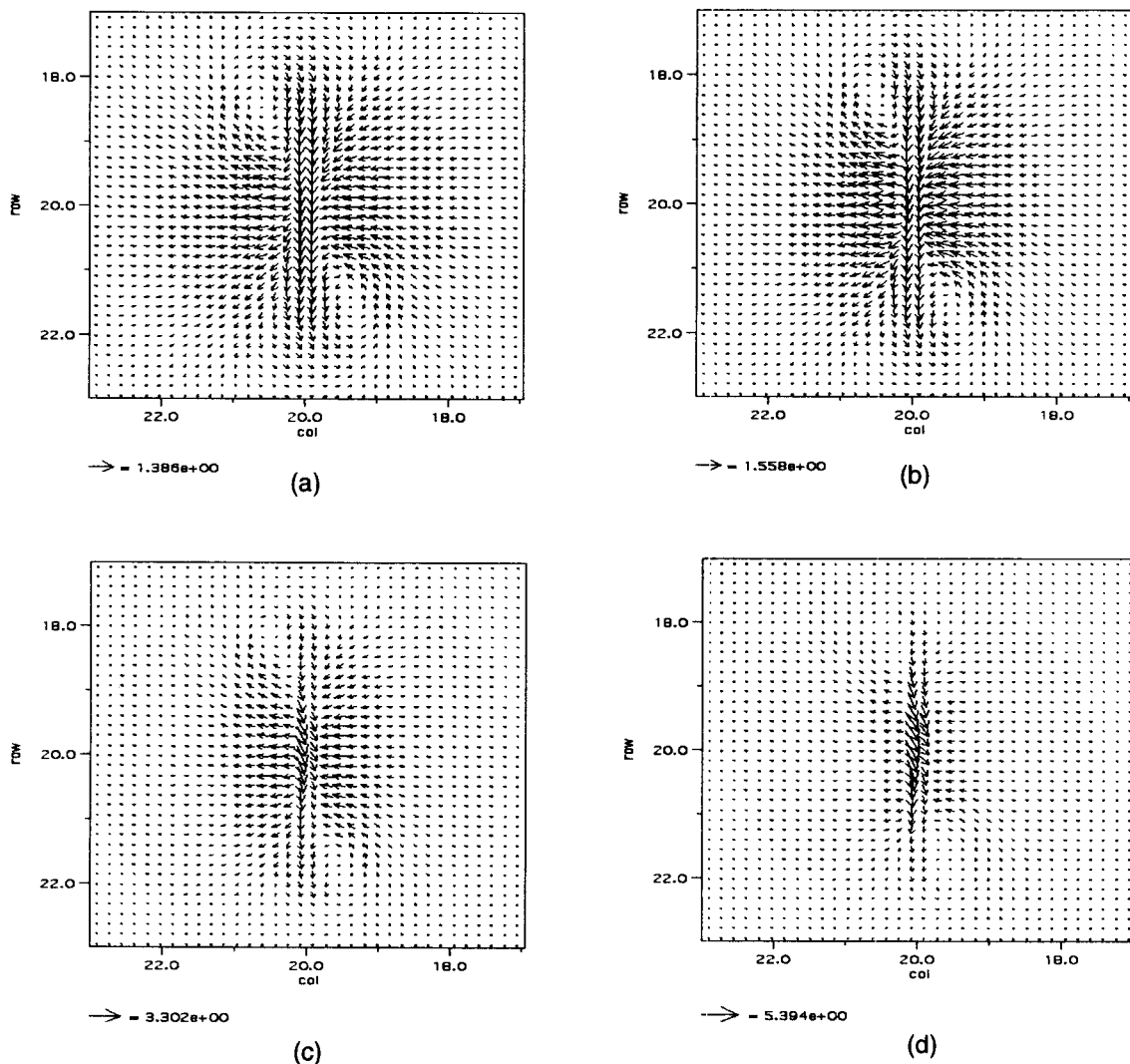


FIG. 12.—Evolution of the transverse magnetic field at  $\{z = 0\}$  for the case  $t_s = 200\tau_A$  at (a)  $t = 450\tau_A$ , (b)  $t = 480\tau_A$ , (c)  $t = 498\tau_A$ , and (d)  $t = 530\tau_A$ . The x-axis (y-axis) runs along the direction named “row” (“col”). [See the electronic edition of the *Journal* for a color version of this figure.]

with no secondary intermediate nonequilibrium bifurcation being produced.

Our results may be relevant to the problem of the initiation of CMEs, as they do show that a global disruption may occur in a magnetic structure with nonzero helicity contents when it is driven into an evolution by the converging motions that have been shown by some observations to be actually present on the photosphere. Let us comment briefly on two different important points, the origin of the helicity and the role of the flux rope, in these events. (1) As we have found that helicity keeps a constant value during the quasi-static phase of evolution, it needs to have been produced during a prior phase. In our simulations, helicity was obtained by twisting motions, but we do not claim that this process actually occurs in the corona; observational evidences for adequate transverse photospheric velocities are still needed. It could as well be a result of processes taking place before the emergence of the structure as also estimated recently by Demoulin et al. (2002) and Nindos & Zhang (2002). We should also note that we cannot exclude that

some amount of helicity be produced by the converging motions themselves, if they are less symmetric than the ones we have considered in our model. (2) Helical structures associated with prominences ejected as part of the CMEs are sometimes observed (but they have not been considered in this paper), and it is clear that twisted ropes are good candidates for the support of cool material. It is still an open problem, however, whether a rope does exist prior to the disruption, thus possibly playing a role in its triggering. Previous three-dimensional results had shown that both a sheared complex topology configuration of the multiarcade type (Antiochos et al. 1999) and a twisted flux rope (Amari et al. 2000) in a nonnecessarily bipolar configuration are candidates for the initiation of a CME. The results presented in this paper complement these earlier ones, by showing an example of an evolving bipolar configuration suffering a major disruption, but without the presence of a twisted flux rope in equilibrium. A rope is created, but only as a result of reconnection during the global disruption, and it is then part of a highly nonequilibrium process. The

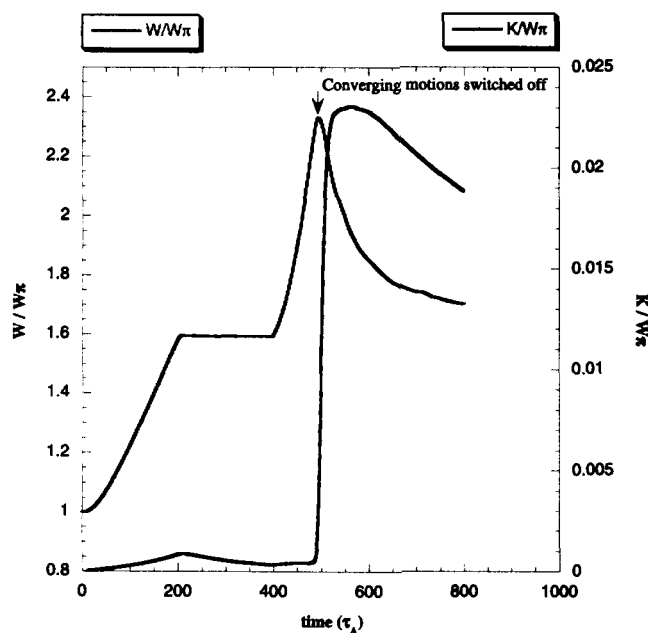


FIG. 13.—Evolution of the magnetic and kinetic energies (in units of  $W_\pi$ ; see text) after the converging boundary velocity field has been switched off, right after the nonequilibrium point, at  $t = 500\tau_A$  seen on the energy curve of Fig. 3 for the case  $t_s = 200\tau_A$ . There is no relaxation toward a neighboring equilibrium even at this stage. [See the electronic edition of the Journal for a color version of this figure.]

results presented here are actually comparable to those obtained for axisymmetric sheared arcades, in which there is a high shear all along the inversion line. Such a shear on a large coherent length scale, impossible to reach in three dimensions by pure vortex motions, has been obtained here thanks to converging motions.

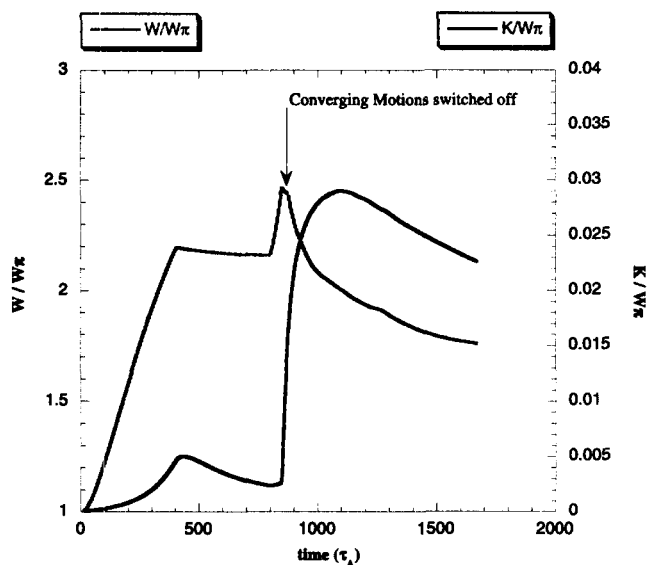


FIG. 14.—Evolution of the magnetic and kinetic energies (in units of  $W_\pi$ ; see text) after the converging boundary velocity field has been switched off (with a linear ramp of  $t = 10\tau_A$ ), in the dip (at  $t = 870\tau_A$ ) of the energy curve of Fig. 3 for the case  $t_s = 400\tau_A$ . No neighboring equilibrium state exists, and a disruption occurs. [See the electronic edition of the Journal for a color version of this figure.]

We acknowledge support from NASA's Sun-Earth Connection Theory Program, NASA's STEREO/SECCHI Consortium, and Centre National d'Etudes Spatiales, which also supported Dr. Amari's visits to SAIC in San Diego. The numerical simulations performed in this paper have been done on the NEC SX5 supercomputer of the IDRIS of the Centre National de la Recherche Scientifique.

#### REFERENCES

- Aly, J. J. 1984, *ApJ*, 283, 349  
 ———. 1990, *Comput. Phys. Commun.*, 59, 13  
 ———. 1991, *ApJ*, 375, L61  
 ———. 1992, *Phys. Fluids B*, 5, 151  
 ———. 1995, *ApJ*, 439, L63  
 Aly, J. J., & Amari, T. 1985, in *Theoretical Problems in High Resolution Solar Physics*, Vol. 212 (Munich: MPA), 319  
 Amari, T., Boulmezaoud, T. Z., & Mikic, Z. 1999a, *A&A*, 350, 1051  
 Amari, T., & Luciani, J. F. 2000, *Phys. Rev. Lett.*, 84, 1196  
 Amari, T., Luciani, J. F., Aly, J. J., & Mikic, Z. 1997, in *Coronal Mass Ejections*, ed. N. Crooker, J. Joselyn, & J. Feynman (Geophys. Monogr. 99; Washington, DC: AGU), 190  
 Amari, T., Luciani, J. F., Aly, J. J., & Tagger, M. 1996a, *A&A*, 306, 913  
 ———. 1996b, *ApJ*, 466, L39  
 Amari, T., Luciani, J. F., & Joly, P. 1999b, *SIAM J. Sci. Stat. Comput.*, 21, 970  
 Amari, T., Luciani, J. F., Mikic, Z., & Linker, J. 1999c, *ApJ*, 518, L57  
 ———. 2000, *ApJ*, 529, L49  
 Antiochos, S. K., DeVore, C. R., & Klimchuk, J. A. 1999, *ApJ*, 510, 485  
 Berger, M. A., & Field, G. B. 1984, *J. Fluid Mech.*, 35, 147  
 Bleybel, A., Amari, T., van Driel-Gesztelyi, L., & Leka, K. 2002, *A&A*, 395, 685  
 Boulmezaoud, T. Z. 1999, Ph.D. thesis, Univ. Paris VI  
 Boulmezaoud, T. Z., & Amari, T. 2000, *Zeitschrift für Angewandte Mathematik und Physik*, 51, 942  
 Burgala, L., Sittler, E., Mariani, F., & Schwenn, R. 1981, *J. Geophys. Res.*, 86, 6673  
 Demoulin, P., Mandrini, C., van Driel-Gesztelyi, L., Thomson, B., Plunkett, S., Kovari, Z., Aulanier, G., & Young, A. 2002, *A&A*, 382, 650  
 DeVore, C. R. 2000, *ApJ*, 539, 944  
 Forbes, T. G. 1991, *Geophys. Astrophys. Fluid Dyn.*, 62, 15  
 Forbes, T. G., & Priest, E. R. 1995, *ApJ*, 446, 377  
 Hagyard, M. 1990, *Mem. Soc. Astron. Italiana*, 61, 337  
 Hagyard, M., Cumings, E., West, E., & Smith, J. 1982, *Sol. Phys.*, 80, 33  
 Inhester, B., Birn, J., & Hesse, M. 1992, *Sol. Phys.*, 138, 257  
 Kaiser, R., Neudert, M., & von Wahl, W. 2000, *Commun. Math. Phys.*, 211, 111  
 Leka, K., Canfield, R. C., McClymont, A. N., & van Driel-Gesztelyi, L. 1996, *ApJ*, 462, 547  
 Linker, J., Lionello, R., Mikic, Z., & Amari, T. 2001, *J. Geophys. Res.*, 106, 25165  
 Low, B. 1994, *Phys. Plasmas*, 1, 1684  
 Machado, M. E., & Moore, R. 1991, *J. Geomag. Geoelectr.*, 43, 1  
 Mikic, Z., & Linker, J. 1994, *ApJ*, 430, 898  
 Nindos, A., & Zhang, H. 2002, *ApJ*, 573, L133  
 Priest, E. R., & Forbes, T. G. 1990, *Sol. Phys.*, 126, 319  
 ———. 2002, *A&A Rev.*, 10, 313  
 Sakurai, T. 1981, *Sol. Phys.*, 69, 343  
 Sturrock, P. A. 1991, *ApJ*, 380, 655  
 Tanaka, K., & Nakagawa, Y. 1973, *Sol. Phys.*, 33, 187  
 Tokman, M., & Bellan, P. 2002, *ApJ*, 567, 1202  
 van Driel-Gesztelyi, L., Schmieder, B., & Baranyi, T. 2002, *Adv. Space Res.*, 29, 1489

## **APPENDIX B**

**“Simulation of CMEs Originating in Active Regions”**

**Z. Mikić, J. A. Linker, P. Riley, and R. Lionello**

**Presented at the Spring AGU/EGS Meeting in Nice, France**

**April 7–11, 2003**

# **SIMULATION OF CMEs ORIGINATING IN ACTIVE REGIONS**

**ZORAN MIKIĆ**

**JON A. LINKER**

**PETE RILEY**

**ROBERTO LIONELLO**

***SCIENCE APPLICATIONS INTL. CORP.  
SAN DIEGO***

**SUPPORTED BY NASA AND NSF**

**Presented at the AGU/EGS Meeting  
Nice, France, April 7–11, 2003**

## **SIMULATION OF CMEs ORIGINATING IN ACTIVE REGIONS**

**Z. Mikić, J. A. Linker, P. Riley, and R. Lionello**

*Science Applications International Corporation, San Diego, California, USA*

Previously, we have addressed the initiation of CMEs by large-scale changes in the solar photospheric magnetic flux. These CMEs had a global nature, since their size was comparable to the solar radius. These early investigations were primarily focused on the theoretical aspects of CME initiation, and the models were thus rather idealized. We will describe recent advances in our computational models that have extended our capability to study localized CMEs, such as those that might originate from an active region. This capability will allow us to analyze actual CME events, and to compare our results in detail with CME observations.

Research supported by NASA and NSF.

## INTRODUCTION

- Simulating CMEs on active-region length scales is challenging
- We have been developing a 3D MHD model for this task
  - Non-uniform meshes
  - 3D finite differences in spherical  $(r, \theta, \phi)$  coordinates
  - Implicit and semi-implicit time differencing
  - Comprehensive physics model including the solar wind and energy transport (radiation, parallel thermal conduction, heating, and Alfvén waves)

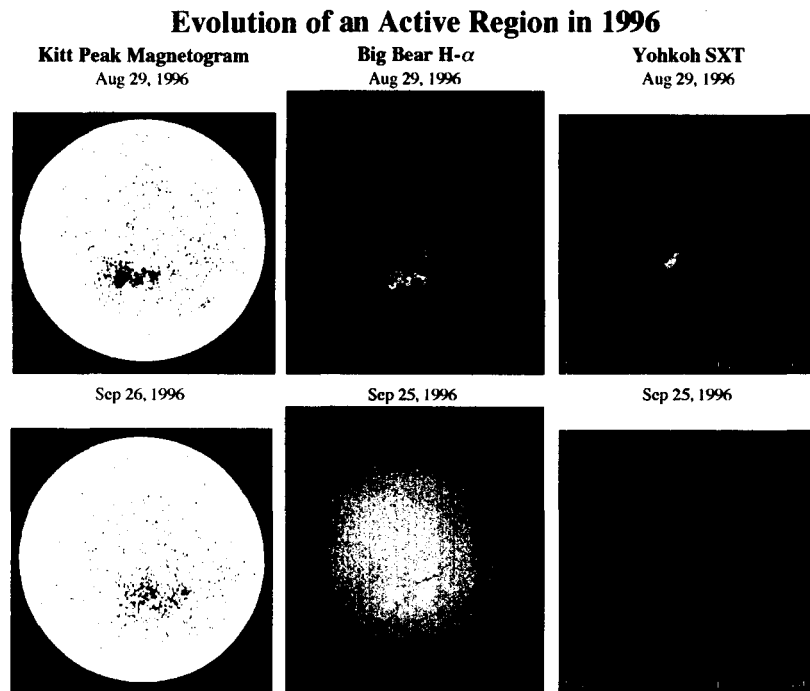
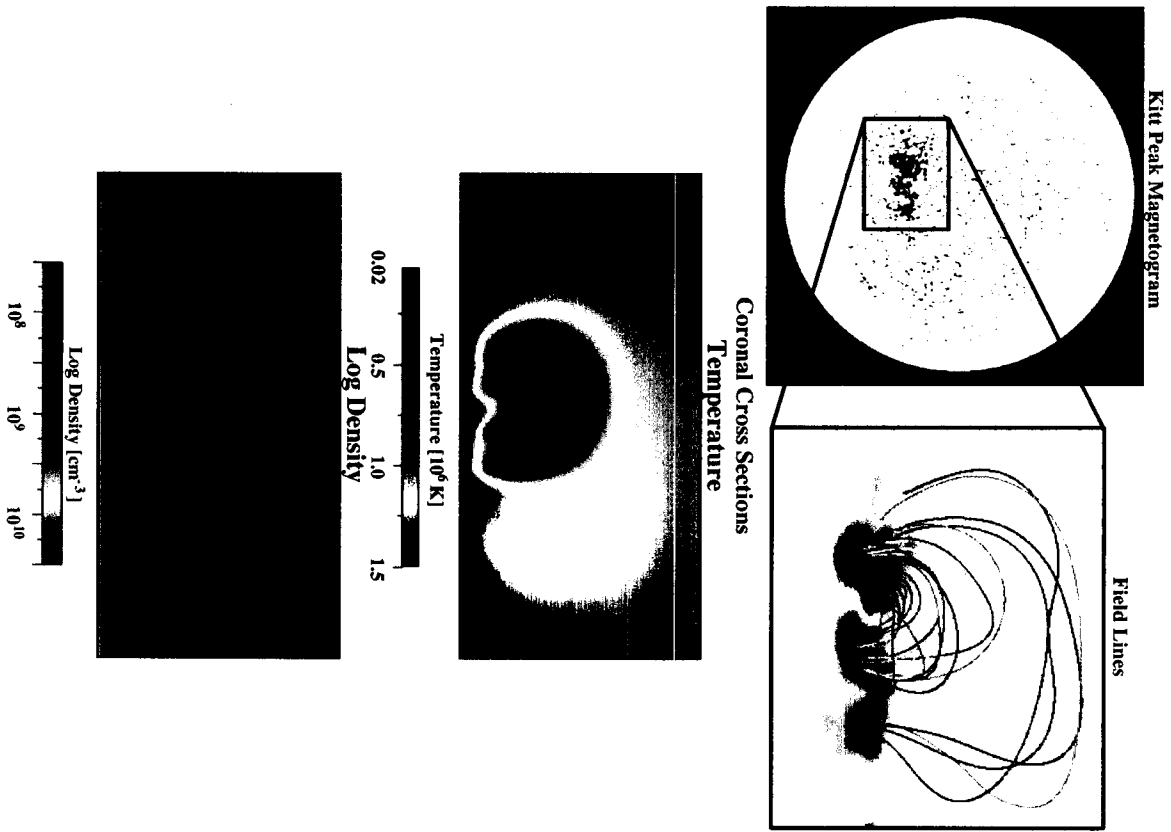


**Figure 4.** Magnetograms, full-disk H- $\alpha$  images, and Yohkoh soft X-ray images of an active region in late August and late September 1996. The two dates are separated by approximately one solar rotation. Note that the H- $\alpha$  images show the presence of a filament. Note also that the magnetic field in the active region has diffused and dispersed from August 29 until September 26. The SXT image shows an S-shape in the active region.

**Figure 1.** Modeling the magnetic and thermal structure of an active region on August 29, 1996. A Kitt Peak magnetogram is used to specify the normal component of the magnetic field. A twist is applied to the field, and the steady state is calculated for a given coronal heating distribution. The temperature and density structure shows that the transition region height varies in different parts of the active region.



## MHD EQUATIONS (POLYTROPIC MODEL)

$$\nabla \times \mathbf{B} = \frac{4\pi}{c} \mathbf{J}$$

$$\nabla \times \mathbf{E} = -\frac{1}{c} \frac{\partial \mathbf{B}}{\partial t}$$

$$\mathbf{E} + \frac{1}{c} \mathbf{v} \times \mathbf{B} = \eta \mathbf{J}$$

$$\frac{\partial \rho}{\partial t} + \nabla \cdot (\rho \mathbf{v}) = 0$$

$$\rho \left( \frac{\partial \mathbf{v}}{\partial t} + \mathbf{v} \cdot \nabla \mathbf{v} \right) = \frac{1}{c} \mathbf{J} \times \mathbf{B} - \nabla p + \rho \mathbf{g} + \nabla \cdot (\nu \rho \nabla \mathbf{v})$$

$$\frac{\partial p}{\partial t} + \nabla \cdot (p \mathbf{v}) = -(\gamma - 1) p \nabla \cdot \mathbf{v}$$

$\gamma = 1.05$  for coronal solution;

$\gamma = 1.5$  for heliospheric solution

## MHD EQUATIONS (IMPROVED ENERGY EQUATION MODEL)

$$\nabla \times \mathbf{B} = \frac{4\pi}{c} \mathbf{J}$$

$$\nabla \times \mathbf{E} = -\frac{1}{c} \frac{\partial \mathbf{B}}{\partial t}$$

$$\mathbf{E} + \frac{1}{c} \mathbf{v} \times \mathbf{B} = \eta \mathbf{J}$$

$$\frac{\partial \rho}{\partial t} + \nabla \cdot (\rho \mathbf{v}) = 0$$

$$\rho \left( \frac{\partial \mathbf{v}}{\partial t} + \mathbf{v} \cdot \nabla \mathbf{v} \right) = \frac{1}{c} \mathbf{J} \times \mathbf{B} - \nabla p - \nabla p_w + \rho \mathbf{g} + \nabla \cdot (\nu \rho \nabla \mathbf{v})$$

$$\frac{\partial p}{\partial t} + \nabla \cdot (p \mathbf{v}) = (\gamma - 1) (-p \nabla \cdot \mathbf{v} - \nabla \cdot \mathbf{q} - n_e n_p Q(T) + H)$$

$$\gamma = 5/3$$

$$\mathbf{q} = -\kappa \hat{\mathbf{b}} \hat{\mathbf{b}} \cdot \nabla T \quad (\text{Close to the Sun, } r \lesssim 10R_s)$$

$$\mathbf{q} = 2\alpha n_e T \hat{\mathbf{b}} \hat{\mathbf{b}} \cdot \mathbf{v} / (\gamma - 1) \quad (\text{Far from the Sun, } r \gtrsim 10R_s)$$

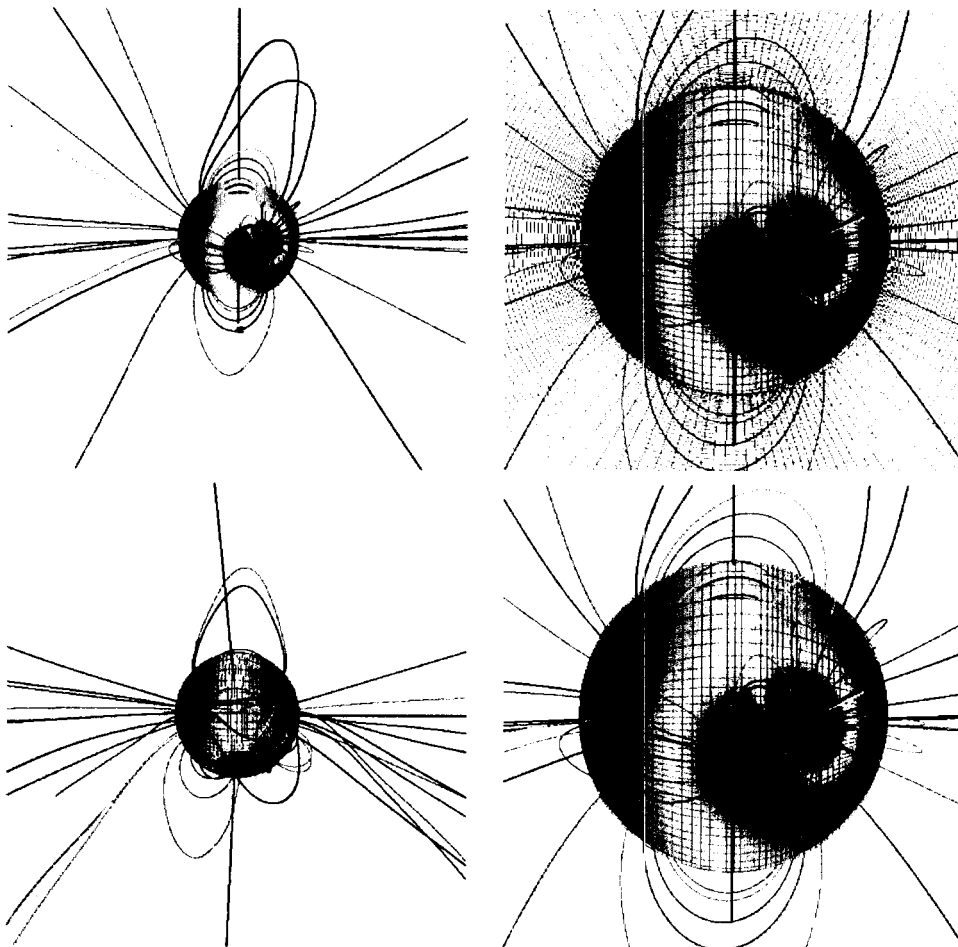
+ WKB equations for Alfvén wave pressure  $p_w$  evolution

## CODE PROPERTIES

- Written in FORTRAN 90
- Designed to run on massively parallel computers using MPI
  - Linux & Beowulf (lf95, pgf90, Intel Fortran)
  - Mac (Absoft)
  - IBM/SP3 (xlf)
- Mesh decomposition among processors in 3D
- We do not use FFTs in  $\phi$ , so that the mesh can be nonuniform
- Dynamic allocation allows mesh size and number of processors to be selected at run time
- Restart capability using HDF files (for long runs)
- Essentially a complete re-write of our spherical 3D MHD Cray code MAS

## EXAMPLE 1: 3D STREAMER

- A typical coarse run takes a few hours on 8–64 processors
- $71 \times 51 \times 51$  mesh on 32 processors on the IBM/SP3 took 2 hours
- Nonuniform meshes with:  
 $\Delta r_{\max}/\Delta r_{\min} \sim 70$ ,  $\Delta \theta_{\max}/\Delta \theta_{\min} \sim 5$ ,  $\Delta \phi_{\max}/\Delta \phi_{\min} \sim 10$
- Dipole magnetic field aligned with the solar rotation axis, together with an added sub-surface dipole to model an active region
- Solar wind with a polytropic energy equation with  $\gamma = 1.05$  and a temperature of  $1.8 \times 10^6$  K and a density of  $10^8 \text{ cm}^{-3}$  in the lower corona



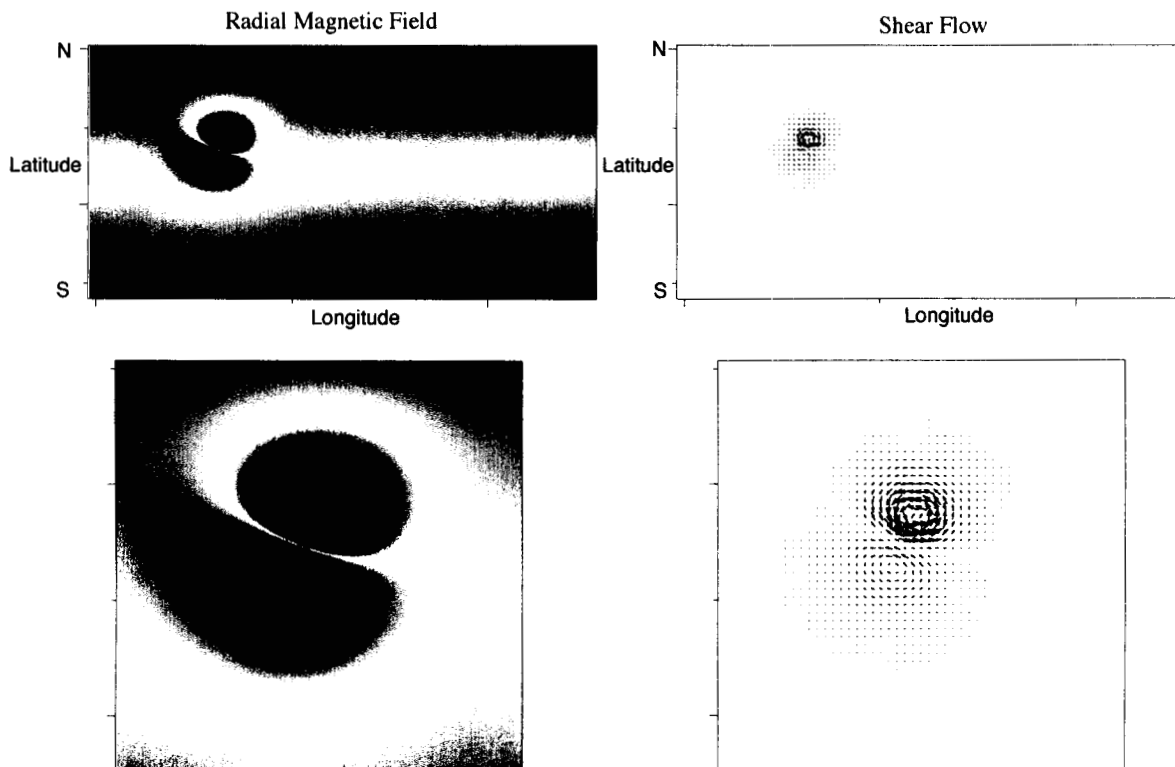
Using Nonuniform Meshes to Simulate a Streamer  
Above an Active Region



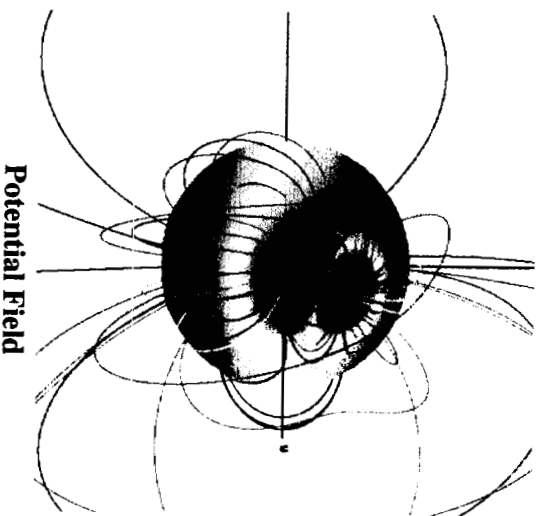
## EXAMPLE 2: SHEARING A MODEL ACTIVE REGION

- Dipole magnetic field aligned with the solar rotation axis, together with an added sub-surface dipole to model an active region
- Start with a potential field
- Apply a shearing flow that preserves  $B_r$ :  
$$\mathbf{v}_{\text{shear}}(\theta, \phi) = \nabla_{\perp} \times \psi \hat{\mathbf{r}}$$
where  $\psi(\theta, \phi) = B_r^2(r = R_o, \theta, \phi)$
- This flow energizes the magnetic field and builds free magnetic energy
- This is in preparation for CME initiation (by continued shear or by flux cancellation)

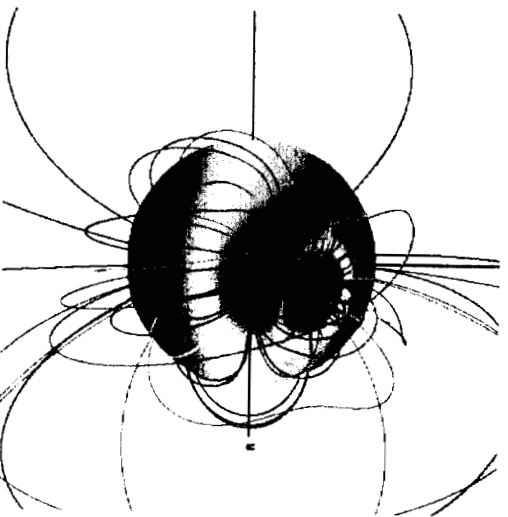
### Localized Shearing of an Active Region



# Shearing an Active Region in a Localized Manner



Potential Field



Sheared Field

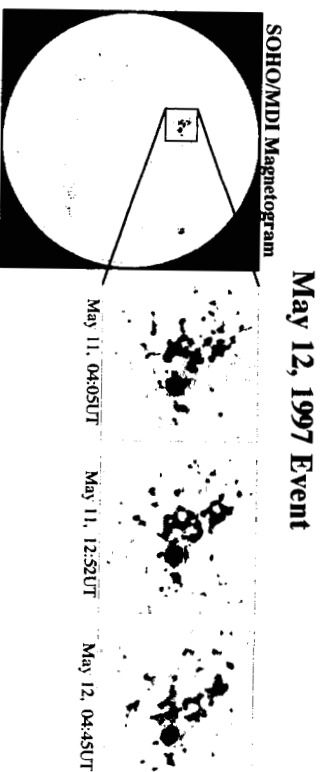


Figure 5. A sequence of MDI magnetograms showing convergence of opposite polarity magnetic near the neutral line flux prior to the launch of the CME.



Figure 7. A sequence of MDI magnetograms for the September 12, 2000 CME. The complex nature of the magnetic field is apparent, as the Sun is approaching solar maximum at this time. The magnetic evolution shows some evidence of flux cancellation and dispersal of the magnetic field in the active region prior to eruption. There is also significant surrounding flux which could lead to rearrangement of the outer field lines. Either the flux cancellation model or the breakout model may be consistent with this event.

## **CONCLUSION**

- The new 3D MHD code runs on parallel computers and is expected to scale well
- The code can be used to perform high-resolution runs ( $300^3$ ) on massively parallel computers
- We have developed the techniques to localize mesh resolution in particular regions (albeit with structured meshes)
- This capability will allow us to simulate a compact CME originating in an active region
- With this capability we can study specific events, allowing detailed comparison with CME observations
- Three possible events that may be studied in the future are a solar minimum event (May 12, 1997), an event during the rising phase of the solar cycle (May 1998), and a solar maximum event (September 12, 2000)

## **APPENDIX C**

**“Parametric Dependence of Coronal Heating Mechanisms and Active-Region Emission”**

**Y. Mok, R. Lionello, Z. Mikić, and J. A. Linker**

**Presented at the Solar Physics Division Meeting, Columbia, Maryland**

**June 16–20, 2003**

# **Parametric Dependence of Coronal Heating Mechanisms and Active-Region Emissions**

**Yung Mok**

Department of Physics & Astronomy  
University of California, Irvine

**Roberto Lionello, Zoran Mikic, Jon Linker**  
Science Applications International Corp., San Diego

Supported by NASA's Sun-Earth Connections Theory Program  
and Supporting Research and Technology Program

## **Abstract**

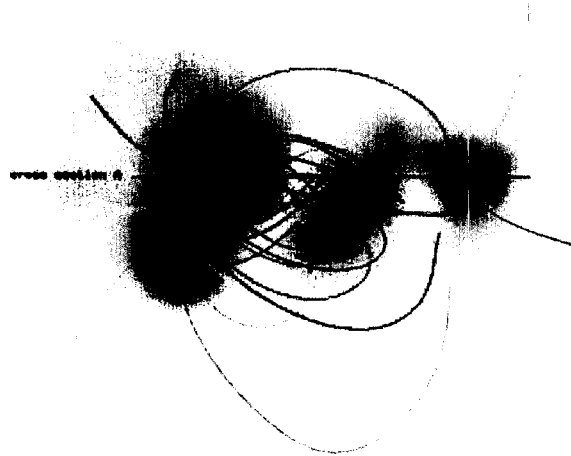
The thermal structure of an active region depends on the mechanism that heats the coronal plasma. A number of coronal heating mechanisms have been proposed over the years. They have different parametric dependence on the magnetic field, plasma density, and possibly other variables. Different mechanisms result in different thermal structures, and therefore, different EUV and soft X-ray emissions from an active region. Hence, the comparison between the computed emissions based on these models and the observed emissions will help to discover the parametric dependence of the actual heating mechanism and put some restrictions on the theoretical models. We have developed a 3D thermomagneto-hydrodynamic code to compute the thermal structure of an active region. The emissions resulted from various heating models will be compared with the images obtained from SOHO and Yohkoh.

## **Objectives of Study**

1. To construct the 3-D thermal structure of an active region
2. To understand how plasma heating affects the thermal structure
3. To compute the EUV and soft X-ray emissions from the structure
4. To demonstrate that the technique we have developed can be used as a possible diagnostics for plasma heating in the corona

## A Model Active Region (7986 of August, 1996) (interpolated and smoothened)

1. A force-free field, generated by shearing the base with a flux-preserving flow, is shown below (top view).
2. The torsion parameter  $\alpha$  of the structure is approximately the same as the one obtained by Madrini et al. (Geofisica International 2000, **39**, 73).



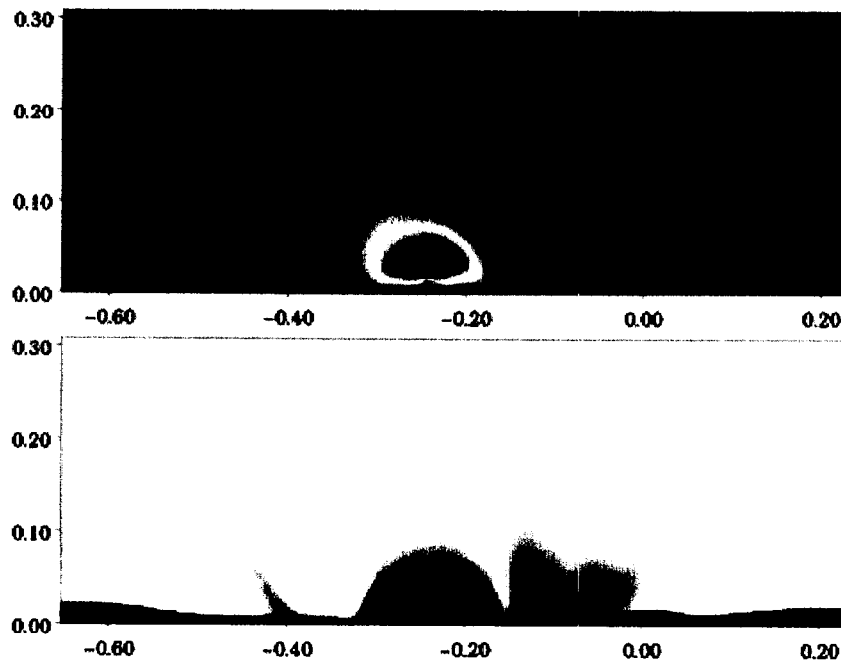
## Important Assumptions and Consequences

1. Magnetic field is sufficiently strong so that the thermal conductivity is finite only along the field.
2. Plasma  $\beta$  is sufficiently small so that the field is relatively rigid and the plasma dynamics is essentially one dimensional. The magnetic structure behaves like an ensemble of static individual field lines.
3. Three models for the plasma heating rate have been investigated:
  - (A) heating  $\sim B^2$ ,                      stochastic energy buildup, current layer dissipation
  - (B) heating  $\sim V_{\text{alfven}}$ ,                magnetic reconnection
  - (C) heating  $\sim \text{density}^2$ ,            a phenomenological model using EIT data fit of isothermal loops (Neupert et al. 1998, SP. 183, 305).
4. For each model, we solve the system of dynamic-energy equations to reach a steady state in order to obtain the 3D profiles of temperature and density. A deep chromosphere in the computation serves as a mass reservoir.

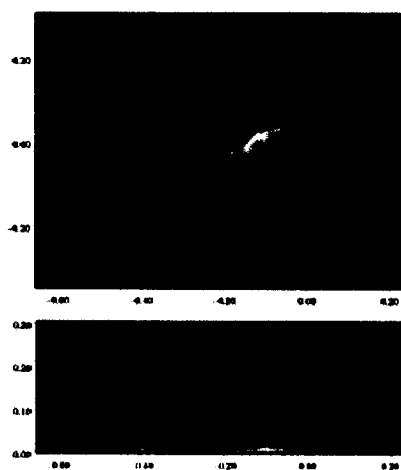
## Emissions from the Computed Thermal Structures

1. EUV emissions at 171, 195 and 284Å are computed by using the SolarSoft routines and the CHIANTI Atomic Database. The instrument response of EIT has also been taken into account. In each case, the emission is integrated along the line of sight. For each heating model and each line, we have computed the expected emission from two different perspectives, a top view as if the structure is at the center of the disk and a side view as if it is at the limb.
2. Soft X-ray emission is also computed from the same perspectives and is integrated along the line of sight. The Yohkoh/SXT instrument response has also been taken into account.
3. In the panels below, we plot the temperature and density profiles at cross section A for each of the heating model to show the details of their vertical structure above the active region. To their right are the EUV and soft X-ray emissions from two perspectives. The familiar SOHO/EIT color scheme is used. (Blue=171Å, Green=195Å, Yellow=284Å).

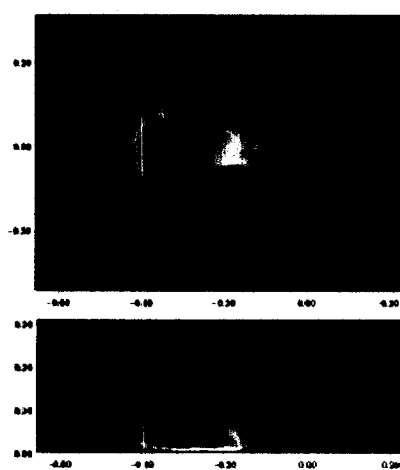
**Model A: heating rate  $\sim B^2$**



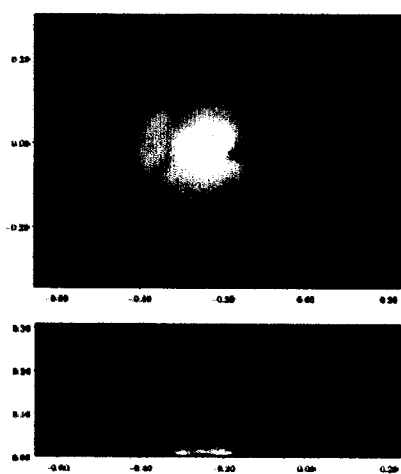
171 A



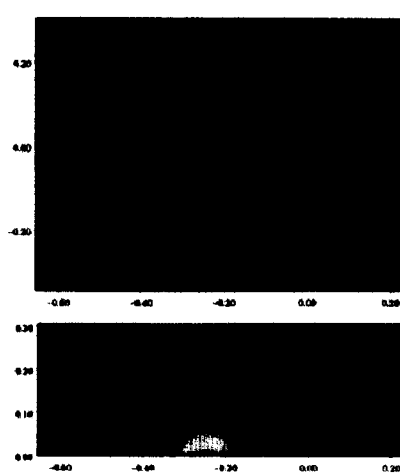
195 A



284 A

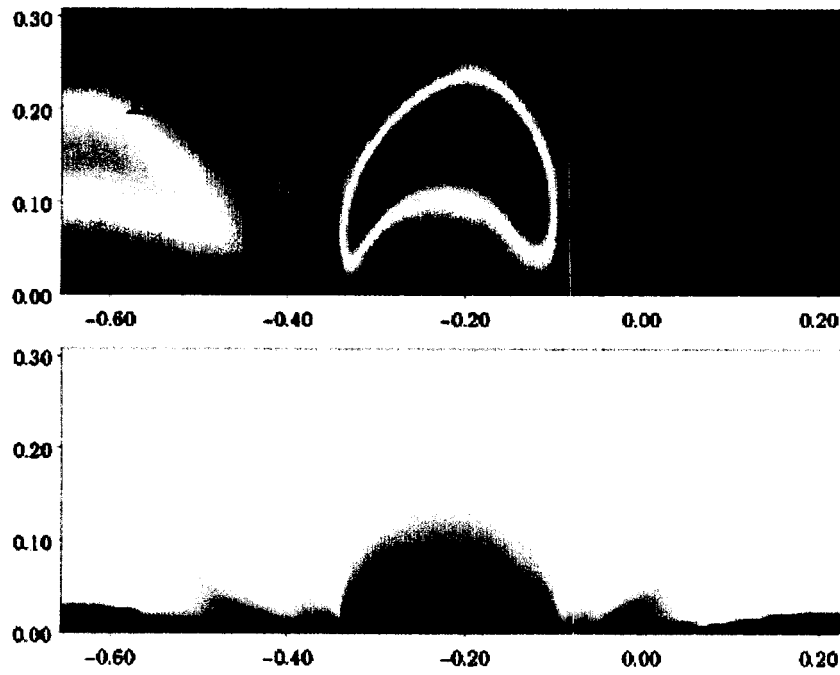


soft X-ray

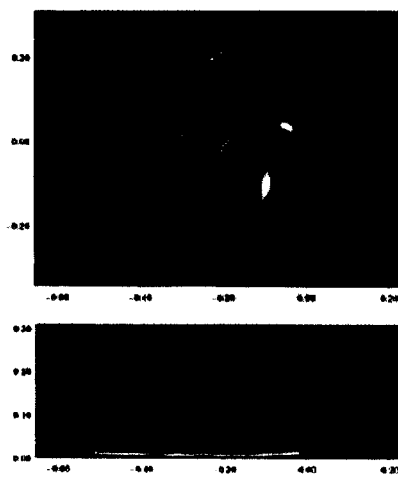




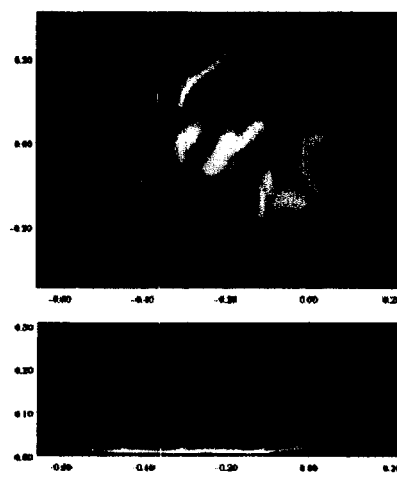
**Model B: heating rate  $\sim V_{\text{alfven}}$**



**171 A**

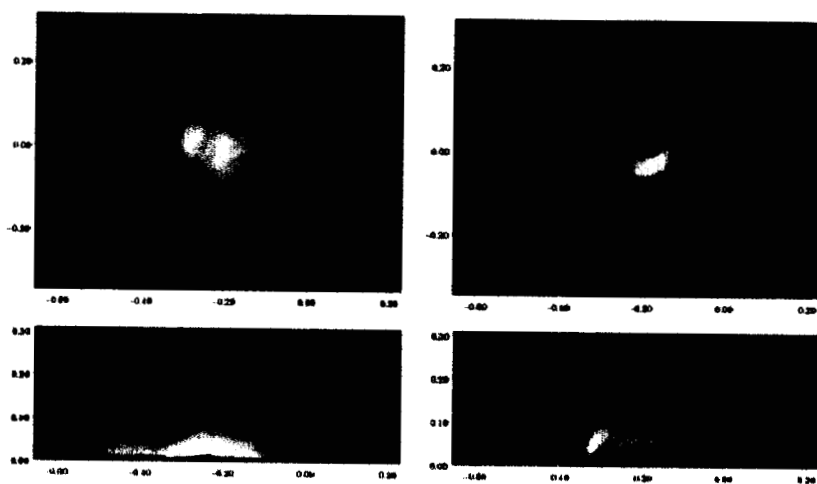


**195 A**

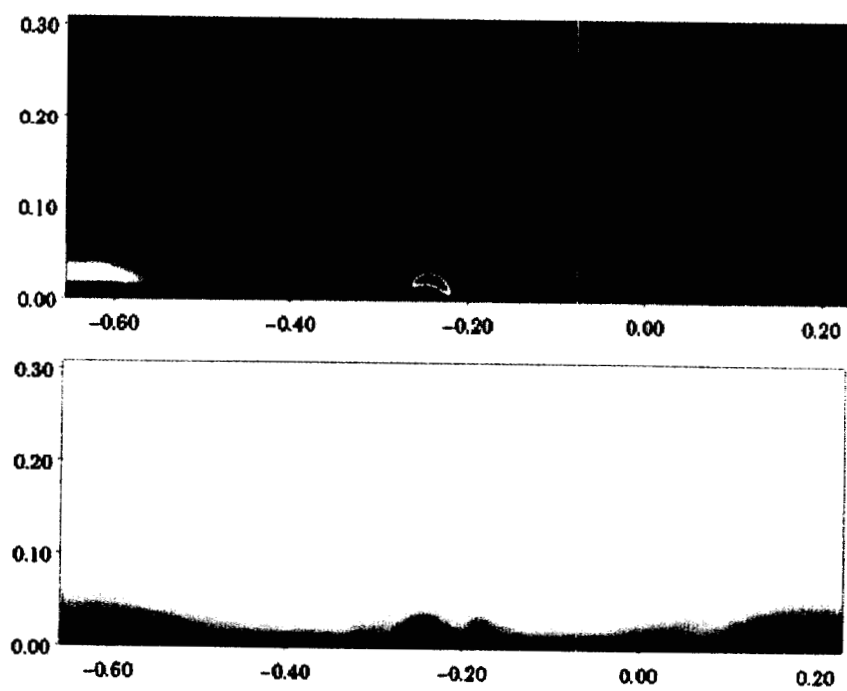


**284 A**

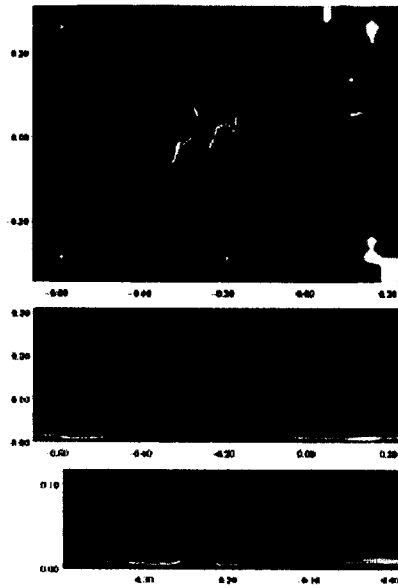
**soft X-ray**



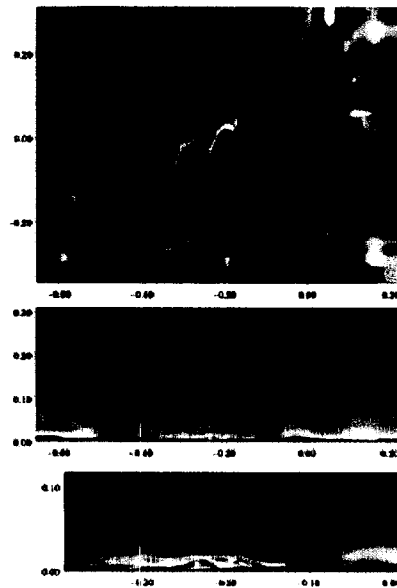
**Model C : heating rate  $\sim (\text{density})^2$**



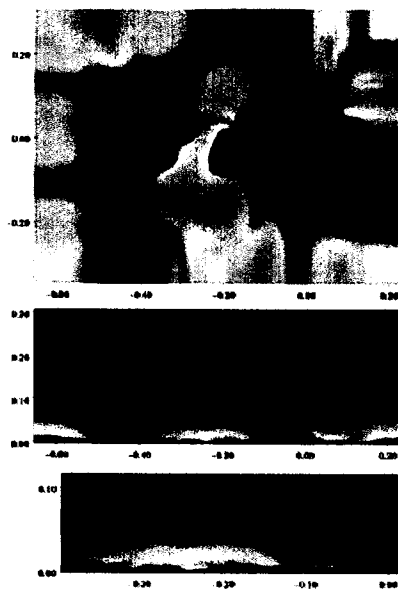
171 A



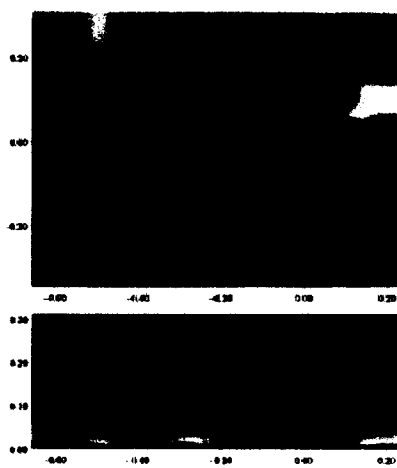
195 A



284 A



soft X-ray



## Preliminary Results + Discussion

1. Different heating models lead to substantially different thermal structures. In model A, the hot region is confined closely to the neighborhood of the magnetic poles, as the heating rate ( $\sim B^2$ ) decreases rapidly with distance. It reaches only to a moderate altitude ( $\sim 0.06$  solar radius). In model B, the hot region reaches to a higher altitude and spans a larger volume because the heating rate ( $\sim V_{\text{Alfven}} \sim B \rho^{-1/2}$ ) decreases more slowly compared to model A. In model C, the hot region is confined to a tiny region above the neutral line because of the rapidly decreasing density above the transition.
2. The density profiles are generally consistent with the temperature profiles at equilibrium according to the gravitational scale height. While the temperature profiles appear to be smooth, the density profiles above the magnetic poles show fine structures. The *fractional* variation in temperature is smaller than the *fractional* variation in density. The fine structures are plasma loops whose field lines are longer than their immediate neighbors, a probable condition in a non-potential field. The longer field line reduces the effectiveness of thermal conduction, resulting in a slightly higher temperature and a longer gravitational scale height at equilibrium.
3. Thin, EUV emitting loops appear naturally due to the elevated density and temperature of these plasma loops. The location and size of these

thin loops are correlated with the high-density region in each model. In model A, the apex is at  $\sim 0.06$  solar radius. It is  $\sim 0.09$  in model B, and ranges from 0.01 to 0.03 in model C. In addition to the thin loops, there are some diffuse EUV loops that reach a higher altitude.

4. The computed soft X-ray images show somewhat diffused features as expected. Some loop-like structures are visible.
5. Limitations of this study -- there are many -- in this first attempt to obtain a 3D thermal structure of an active region:
  - A. Vector magnetograms are not available for this case. Therefore, there are uncertainties about the geometry of the field lines, which critically determine the direction of heat flow. Future technology should provide more reliable information about the field so that the computed thermal structure is more realistic.
  - B. The magnetogram has been highly smoothened and interpolated in the simulation so that it can be handled in a  $127 \times 89 \times 127$  mesh. The fine structures in the field are lost. Therefore, it is not possible to reproduce the multiple fine loops as seen in the actual SOHO/EIT and Yohkoh/SXT images. The original, unprocessed magnetogram would have required more grid points than that can be handled practically.
  - C. The sharp density-temperature gradients in the transition region require very fine vertical mesh to resolve, making the computation very time consuming. As a result, approximations must be made to make the computation practical and within our

computing resources. We have attempted to minimize the numerical errors, but it can still be improved. The code is being ported to massively parallel environment, and faster hardwares will greatly improve the accuracy of the results.

- D. The computed images from the three models cannot consistently match the actual ones across all wavelengths. This is not completely surprising because of the uncertainties in the input and the approximations we have to make in this first attempt. In addition, other plausible models have not been considered. Nevertheless, we have developed the framework and the tools needed for future works that will address these issues. Stay tuned.

# REPORT DOCUMENTATION PAGE

Form Approved  
OMB No. 0704-0188

Public reporting burden for this collection of information is estimated to average 1 hour per response, including the time for reviewing instructions, searching existing data sources, gathering and maintaining the data needed, and completing and reviewing the collection of information. Send comments regarding this burden estimate or any other aspect of this collection of information, including suggestions for reducing this burden, to Washington Headquarters Services, Directorate for Information Operations and Reports, 1215 Jefferson Davis Highway, Suite 1204, Arlington, VA 22202-4302 and to the Office of Management and Budget, Paperwork Reduction Project (0704-0188), Washington, DC 20508.

1. AGENCY USE ONLY (Leave Blank)		2. REPORT DATE October 7, 2003	3. REPORT TYPE AND DATES COVERED 1st Year 1st Semi-Annual Progress Report 1/14/03-7/13/03
4. TITLE AND SUBTITLE Modeling the Magnetic and Thermal Structure of Active Regions: 1st Year 1st Semi-Annual Progress Report			5. FUNDING NUMBERS NAS5-03008
6. AUTHORS Zoran Mikic			
7. PERFORMING ORGANIZATION NAME(S) AND ADDRESS(ES) Science Applications International Corporation 10260 Campus Point Drive San Diego, CA 92121-1578			8. PERFORMING ORGANIZATION REPORT NUMBER SAIC-03/8013:APPAT-322 01-0157-04-6811-000
9. SPONSORING/MONITORING AGENCY NAME(S) AND ADDRESS(ES) NASA Headquarters Operation Office Goddard Space Flight Center Greenbelt, MD 20771			10. SPONSORING/MONITORING AGENCY REPORT NUMBER
11. SUPPLEMENTARY NOTES			
12a. DISTRIBUTION/AVAILABILITY STATEMENT			12b. DISTRIBUTION CODE
13. ABSTRACT (Maximum 200 words)  This report details progress during the first half of the first year of the Solar Physics Supporting Research & Technology contract, "Modeling the Magnetic and Thermal Structure of Active Regions."			
14. SUBJECT TERMS Solar Corona, Coronal Magnetic Field, Heliosphere, Magnetohydrodynamics			15. NUMBER OF PAGES 37
			16. PRICE CODE
17. SECURITY CLASSIFICATION OF REPORT UNCLASSIFIED	18. SECURITY CLASSIFICATION OF THIS PAGE UNCLASSIFIED	19. SECURITY CLASSIFICATION OF ABSTRACT UNCLASSIFIED	20. LIMITATION OF ABSTRACT UL

NSN 7540-01-280-5500

Computer Generated

STANDARD FORM 298 (Rev 2-89)  
Prescribed by ANSI Std Z39-18  
298-102